

Erik Jonsson School of Engineering and Computer Science

*Assessing State-of-the-Art Capabilities for Probing the
Atmospheric Boundary Layer: The XPIA Field Campaign*

UT Dallas Author(s):

Ryan Ashton
Mithu Debnath
Armita Hamidi
Giacomo V. Iungo

Rights:

©2017 American Meteorological Society

Citation:

Lundquist, Julie K., James M. Wilczak, Ryan Ashton, Laura Bianco, et al. 2017. "Assessing state-of-the-art capabilities for probing the atmospheric boundary layer: The XPIA field campaign." *Bulletin of the American Meteorological Society* 98(2): 289-314, doi:10.1175/BAMS-D-15-00151.1

This document is being made freely available by the Eugene McDermott Library of the University of Texas at Dallas with permission of the copyright owner. All rights are reserved under United States copyright law unless specified otherwise.

ASSESSING STATE-OF-THE-ART CAPABILITIES FOR PROBING THE ATMOSPHERIC BOUNDARY LAYER

The XPIA Field Campaign

JULIE K. LUNDQUIST, JAMES M. WILCZAK, RYAN ASHTON, LAURA BIANCO, W. ALAN BREWER, ADITYA CHOUKULKAR, ANDREW CLIFTON, MITHU DEBNATH, RUBEN DELGADO, KATJA FRIEDRICH, SCOTT GUNTER, ARMITA HAMIDI, GIACOMO VALERIO IUNGO, ALEYA KAUSHIK, BRANKO KOSOVIĆ, PATRICK LANGAN, ADAM LASS, EVAN LAVIN, JOSEPH C.-Y. LEE, KATHERINE L. MCCAFFREY, ROB K. NEWSOM, DAVID C. NOONE, STEVEN P. ONCLEY, PAUL T. QUELET, SCOTT P. SANDBERG, JOHN L. SCHROEDER, WILLIAM J. SHAW, LYNN SPARLING, CLARA ST. MARTIN, ALEXANDRA ST. PE, EDWARD STROBACH, KEN TAY, BRIAN J. VANDERWENDE, ANN WEICKMANN, DANIEL WOLFE, AND ROCHELLE WORSNOP

New measurement technologies provide exciting opportunities to advance understanding of complex flows in the atmospheric boundary layer. The XPIA campaign assessed innovative deployment strategies to offer guidance for future studies.

Wind energy now provides 20% of the electricity in some regions of the United States, with promise to provide far more (Wiser et al. 2015). Individual wind turbines generate power based on the winds entering their rotor disk; similarly, clusters of wind turbines, or wind farms, respond to winds and turbulent characteristics of the atmospheric boundary layer (ABL; Sumner and Masson 2006; Wharton and Lundquist 2012; Vanderwende and Lundquist 2012; Sathe et al. 2013) as well as mesoscale flow features (Cui et al. 2015). In turn, wind farms generate complex local wind flows characterized by increased turbulent mixing, modified wind profiles at wind turbine rotor disk heights, and accelerations beneath wind turbines (Barthelmie et al. 2007; Fitch et al. 2013; Rajewski 2013; Rhodes and Lundquist

2013). These complex flows affect local meteorology and downwind turbines. To optimize wind energy deployment and production, and to assess wind farm impacts, accurate measurements of the complex flows within and around wind farms are required.

Emerging measurement capabilities may provide the capabilities for assessing these complex flows. Avoiding the limitations of fixed meteorological towers, Doppler lidar, radar, and sodar sensing systems have assessed wind turbine inflow and wakes (Käsler et al. 2010; Bingöl et al. 2010; Hirth and Schroeder 2013; Smalikho et al. 2013; Iungo et al. 2013; Aitken et al. 2014; Iungo and Porté-Agel 2014; Aitken and Lundquist 2014; Kumer et al. 2015; Trabucchi et al. 2015; Hirth et al. 2015; Banta et al. 2015); a comprehensive review is given in Clifton et al. (2015). Coordinated measurements with

multiple Doppler systems can provide vector winds (Newsom et al. 2008; Hill et al. 2010; Carbajo Fuertes et al. 2014; Berg et al. 2015; Gunter et al. 2015; Klein et al. 2015) in the boundary layer. Microwave radiometers provide frequent high-resolution assessments of temperature stratification to assess atmospheric stability (Ware et al. 2003; Bianco et al. 2005; Cimini et al. 2011; Friedrich et al. 2012). Two-component vector wind fields can be estimated over large areas using a single non-Doppler elastic backscatter lidar (Mayor and Eloranta 2001; Hamada et al. 2016).

In tandem with these advances in measurements, the development of high-resolution wind turbine wake simulation capabilities (Porté-Agel et al. 2011; Churchfield et al. 2012; Mirocha et al. 2014; Dörenkämper et al. 2015; Bhaganagar and Debnath 2015) and means for nesting these simulations within mesoscale models to accommodate variable forcing (Muñoz-Esparza et al. 2014, 2015) suggests that the coupling of measurements and simulation capabilities will enable the development of new types of model–data integration. Beyond describing phenomena associated with wind farms, new observational capabilities may assess the numerical simulations that are increasingly being used to predict and optimize flow within wind farms. Further, instrument simulators within simulation tools (Stawiarski et al. 2013; Wainwright et al. 2014; Lundquist et al. 2015) can help to assess the abilities of measurements to probe challenging scientific questions regarding the rapid evolution of inhomogeneous flows such as wind turbine wake meandering (España et al. 2011; Howard et al. 2015). As more remote sensing systems are deployed offshore, on buoys, tests with motion tables (Mathisen 2013) prove useful for quantifying the error of these systems.

The confluence of these emerging measurement and computational capabilities suggests that the integration of simulations and observations can create new tools to enable the exploration of new scientific questions that have previously been out of our reach. Before this goal can be realized, we must assess the capabilities of these new measurement approaches. To achieve a coupling of measurements and simulations, we must define the measurement uncertainty of these platforms, especially under multi-instrument coordinated scanning scenarios.

To assess the capabilities for quantifying features of the complex flow in and near wind farms, the U.S. Department of Energy sponsored the eXperimental Planetary boundary layer Instrumentation Assessment (XPiA) campaign at the Boulder Atmospheric Observatory (BAO), held 2 March–31 May 2015. The spring season offers a range of wind speed, direction, and precipitation conditions to challenge the instrumentation. XPiA was supplemented by the National Science Foundation (NSF)-sponsored “Characterizing the Atmospheric Boundary Layer” (CABL) educational outreach project, which provided in situ sensors such as radiosonde launches, 12 sonic anemometers deployed on the 300-m tower, and two surface flux stations, as well as opportunities to engage students from middle school through graduate studies. In addition to deploying state-of-the-art wind scanning remote sensing technology, such as Ka-band radars and scanning lidars, the XPiA team developed and tested multi-Doppler scanning techniques for comparison to the in situ instrumentation. To quantify the uncertainty of these new types of measurements, results of these scans and retrievals are compared to standard measurements as well as to profiles from profiling lidars. In addition, radiosonde launches, along with temperature and

AFFILIATIONS: LUNDQUIST—Department of Atmospheric and Oceanic Sciences, University of Colorado Boulder, Boulder, and National Renewable Energy Laboratory, Golden, Colorado; WILCZAK, BREWER, CHOUKULKAR, MCCAFFREY, SANDBERG, AND WEICKMANN—National Oceanic and Atmospheric Administration/Earth System Research Laboratory, Boulder, Colorado; ASHTON, DEBNATH, HAMIDI, AND IUNGO—The University of Texas at Dallas, Dallas, Texas; BIANCO AND WOLFE—Cooperative Institute for Research in Environmental Sciences, University of Colorado Boulder, Boulder, Colorado; CLIFTON—National Renewable Energy Laboratory, Golden, Colorado; DELGADO, LANGAN, LASS, LAVIN, SPARLING, ST. PE, AND STROBACH—University of Maryland, Baltimore County, Baltimore, Maryland; FRIEDRICH, KAUSHIK, LEE, QUELET, ST. MARTIN, TAY, VANDERWENDE, AND WORSNOP—Department of Atmospheric and Oceanic Sciences, University of Colorado Boulder, Boulder, Colorado; GUNTER AND SCHROEDER—Texas Tech University, Lubbock,

Texas; KOSOVIC AND ONCLEY—National Center for Atmospheric Research, Boulder, Colorado; NEWSOM AND SHAW—Pacific Northwest National Laboratory, Richland, Washington; NOONE—College of Earth, Ocean and Atmospheric Sciences, Oregon State University, Corvallis, Oregon

CORRESPONDING AUTHOR E-MAIL: Julie K. Lundquist, julie.lundquist@colorado.edu

The abstract for this article can be found in this issue, following the table of contents.

DOI:10.1175/BAMS-D-15-00151.1

A supplement to this article is available online (10.1175/BAMS-D-15-00151.2)

In final form 8 June 2016

©2017 American Meteorological Society

moisture profiles from the tower, provide verification data for assessing microwave radiometer estimates of atmospheric stability.

Herein, we summarize the XPIA field experiment design, highlight novel approaches to boundary layer measurements, and quantify the measurement uncertainties associated with these experimental methods. We first detail the instruments deployed during XPIA. We then discuss lidar measurement techniques and their uncertainties, progressing from long-duration multi-Doppler stares at sonic anemometers to more rapid scans and larger volumes. Next, we evaluate dual-Doppler retrievals from Ka-band Doppler radars by comparison to tower anemometry and profiling lidar. We then evaluate means for retrieving 3D volumes with multiple scanning systems. Subsequently, we quantify the skill of microwave radiometers to assess atmospheric stability. Finally, we highlight time periods that could be useful for large-eddy simulation or mesoscale model validation.

FIELD EXPERIMENT DESIGN. The XPIA field experiment design, as well as instrument performance, is discussed in detail in Lundquist et al. (2017, forthcoming NREL technical report). Here we present an overview of the instruments. The experiment was conducted from 2 March to 31 May 2015 at BAO, located ~25 km east of the eastern slopes of the Rocky Mountains, ~25 km north of downtown Denver, Colorado, and ~20 km east-northeast of Boulder, Colorado, at an elevation of 1,584 MSL (Fig. 1). The centerpiece of the BAO facility was its 300-m meteorological tower. XPIA instruments were deployed on or near the tower and up to 4 km offsite. A summary of the data availability for most instruments for the entire experiment appears as Table ES1 in the supplemental material (which can be found online at <http://dx.doi.org/10.1175/BAMS-D-15-00151.2>).

BAO tower. Constructed in 1977, the BAO was a unique and valuable research facility for studying the planetary boundary layer (Kaimal and Gaynor 1983). The 300-m-tall, guyed, open-lattice structure had a uniform triangular cross section; the legs of the tower were spaced 3 m apart. It was regularly instrumented at 10, 100, and 300 m above ground level (AGL) with wind, temperature, and relative humidity measurements. During XPIA, two 3D sonic anemometers (Campbell CSAT3) were deployed at each of six levels (50, 100, 150, 200, 250, and 300 m AGL) for 12 total sonic anemometers with measurement resolution (offset error) generally less than 1×10^{-3} (8×10^{-2}) m s^{-1} in the horizontal and 5×10^{-4} (4×10^{-2}) m s^{-1} in the vertical. Anemometers

were mounted on booms pointing northwest (NW, 334°) and southeast (SE, 154°). Most booms were 4.3 m long; at the 250-m level, the SE boom was only 3.3 m, shorter than would be required to avoid flow distortion according to the International Electrotechnical Commission (IEC) standard for boom mounting of anemometers (IEC 2005). Data subject to tower wakes, defined by McCaffrey et al. (2016b), are excluded for winds between 111° and 197° for the northwest sonic and 299° to 20° for the southeast sonic. Since there were no significant upstream effects from the tower, there was always at least one unwaked sonic at each level. Following the experiment, we applied a tilt-correction algorithm using the planar fit method (Wilczak et al. 2001) to all sonic anemometer data. Six temperature/relative humidity sensors measured vertical profiles of temperature and moisture on the SE booms of the 300-m tower. These sensors were based on a Sensiron SHT75 solid-state sensor that was housed in an aspirated double-tube shield optimized for low-power operation (Horst et al. 2016). These sensors were individually calibrated and, with this shield, accuracy of better than 0.1 K is expected. Finally, at the base of the tower, a tipping-bucket rain gauge quantified precipitation; a standard pressure measurement was also available.

Vertically profiling lidar (lidar supersite). During XPIA, six lidars were deployed approximately 100 m directly south of the BAO tower at a location called the lidar supersite (LSS). Five of these lidars were vertically profiling units, while the sixth was a scanning lidar utilized primarily in profiling mode.

The LSS systems included two Leosphere/NRG WINDCUBE, version 1 (v1) profiling lidars (WC68, WC61) that were deployed by the University of Colorado Boulder and the National Center for Atmospheric Research (NCAR)'s Research Applications Laboratory (Aitken et al. 2012; Rhodes and Lundquist 2013). These profiling lidars sample line-of-sight (LOS) velocities sequentially in four cardinal directions along a nominally 28° azimuth from vertical, simultaneously sampling 10 range gates centered on 40, 60, 80, 100, 120, 140, 160, 180, 200, and 220 m AGL. This approach assumes homogeneity for 4 s across the cone defined by the four beams; the resulting uncertainty can be quantified in complex terrain (Bingöl et al. 2009) and inhomogeneous flow (Rhodes and Lundquist 2013; Lundquist et al. 2015). These lidars were available from 1 March (4 March for WC61) past the end of the experiment and did not move.

Similarly, the Leosphere WINDCUBE Offshore 8.66 profiling lidar (WCv2) samples LOS velocities in four cardinal directions along a nominally 28° azimuth

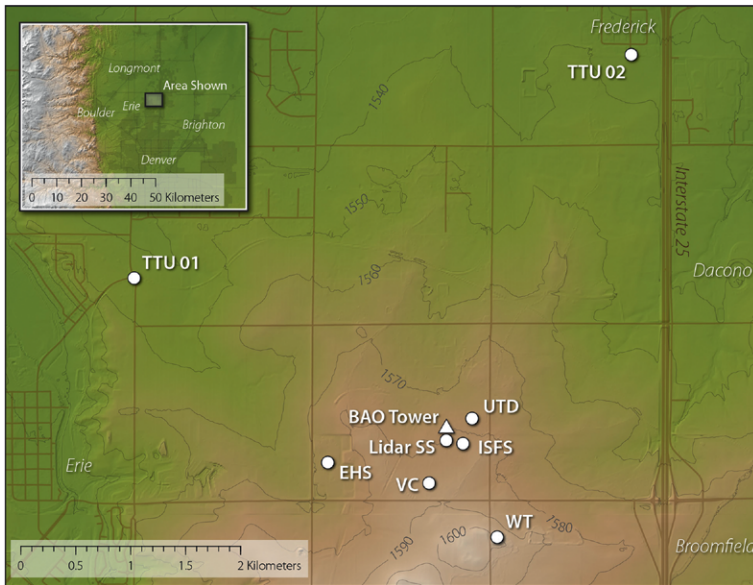


FIG. 1. Schematic diagram of the XPIA deployment. The location of the BAO 300-m tower (BAO Tower); the lidar supersite (Lidar SS); the Visitor Center (VC), location of NOAA Dalek 2, the radar wind profiler/RASS systems, the NOAA and University of Colorado Boulder (CU) microwave radiometers, and several radiosonde launches; the Water Tank (WT), location of the NOAA HRDL, the UMBC lidar and radiometer, and some radiosonde launches; Erie High School (EHS), location of the NOAA Dalek 1; and UTD, the location of the UTD 200S lidar, and the locations of the two TTU Ka-band Doppler radars (TTU 01, TTU 02). Contours show elevation in meters above sea level. (inset) The location of the instrument deployment's XPIA measurement site in northern Colorado.

from vertical, followed by a fifth vertically pointed beam. Range gates were centered on 40, 50, 60, 80, 100, 120, 140, 150, 160, 180, and 200 m AGL. The WCv2 was located at the lidar supersite from 12 March to 8 June 2015. On 24–28 May, it was placed on the University of Maryland, Baltimore County (UMBC) motion table (see “Motion platform” for more information). The WCv2 includes a motion-compensation algorithm based on independent GPS measurements.

AXYS Technologies, Inc. deployed and operated two Vindicator III profiling Doppler lidars (units 3013 and 3015) at the lidar supersite from 30 March to 29 May 2015. These lidars use three separate outgoing laser beams (split from a single source); each beam makes an angle of 15° from the vertical (i.e., 75° in elevation). During XPIA, both Vindicators were configured using range gates centered on 55, 60, 80, 100, 120, and 150 m AGL.

A Halo Photonics Streamline Doppler lidar on loan from the U.S. Department of Energy (DOE) Office of Science Atmospheric Radiation Measurement (ARM) program (Pearson et al. 2009; Newsom 2012; Mather and Voyles 2013) was deployed at the lidar

supersite from 6 March to 16 April 2015. The Halo incorporates a full upper-hemispheric scanner. During XPIA, the Halo used a 1-s pulse accumulation time, a range-gate size of 30 m, and 200 range gates. The typical maximum range during XPIA was between 1 and 3 km. During XPIA, the Halo was configured using a fixed scan schedule, consisting of a 40-s plan-position-indicator (PPI) scan at an elevation angle of 60° performed once every 12 min, a 10-min tower stare once per hour, a target sector scan once per day to confirm heading relative to the tower, and vertical stares otherwise. Because of this regular scanning schedule, it is included in the discussion of the LSS rather than in the scanning lidar discussion below.

Scanning lidar. Coherent Doppler lidars enable wind measurements throughout the boundary layer in regions that may be difficult to sample with traditional instruments such as meteorological towers (Sanz Rodrigo et al. 2013). In contrast to anemometers on tall masts that characterize wind

shear, veer, and turbulence over different heights at a fixed location (Walter et al. 2009), scanning Doppler lidars characterize the spatial variability of the wind field across large wind farms, demanding methods for sampling larger volumes. Doppler lidars allow flexible measurement strategies without changing the deployment location of the instrument, and have thus been used to measure the variability of wind turbine wakes from the ground (Käsler et al. 2010; Smalikho et al. 2013; Iungo et al. 2013; Aitken et al. 2014; Iungo and Porté-Agel 2014) and from turbine nacelles (Bingöl et al. 2010; Aitken and Lundquist 2014), as well as sampling the flow entering a turbine disk for feed-forward control (Schlipf et al. 2013; Mikkelsen et al. 2013) and wind resource assessment (Krishnamurthy et al. 2013). Turbulence metrics from lidar are also being explored (Sathe and Mann 2013).

During XPIA, five scanning Doppler lidars with variable scanning strategies were deployed in and around the BAO field site (Fig. 1). These instruments included four Leosphere 200S systems [National Oceanic and Atmospheric Administration (NOAA) Dalek 1, NOAA Dalek 2, The University of Texas at

Dallas (UTD), and UMBC] and the NOAA high-resolution Doppler lidar (HRDL), as described in Table 1. The 200S scanning Doppler lidar operates with a 1.54- μm wavelength eye-safe laser with a pulse energy of 0.1 mJ. The systems were run in either 0.5- or 1-s accumulation time mode, resulting in data sampling rates of 2 or 1 Hz. In addition, the pulse width can be adjusted to provide range-gate sizes of 25, 50, 75, or 100 m, with corresponding pulse durations of 100, 200, 300, or 400 ns. NOAA's HRDL is a scanning, pulsed, coherent Doppler lidar developed at the NOAA/Earth System Research Laboratory (ESRL)/Chemical Sciences Division, operating with a 2.0218- μm laser (Grund et al. 2001). With a 200-ns pulse width and 30-m range gates, HRDL has provided insight into boundary layer dynamics (Banta et al. 2002) and wind turbine wakes (Smalikhov et al. 2013; Aitken et al. 2014; Banta et al. 2015), among other phenomena.

Ka-band scanning radar. The two Texas Tech University Ka mobile Doppler radars (TTUKa1 and TTUKa2; Hirth and Schroeder 2013; Hirth et al. 2015) were deployed at XPIA from 4 March to 4 April 2015. Throughout the experiment, the pulse repetition frequency (15 kHz), pulse width (20 ms), and range resolution (15 m) were maintained, while the scan speed varied based on the atmospheric conditions but was always much faster than the scanning lidars. TTUKa1 (TTUKa2) was deployed 3.1 km (3.8 km) northwest (north) of the BAO tower (Fig. 1). Considering the 0.33° half-power beamwidth of the radars, these distances yielded an azimuthal resolution of 18 m (22 m) for TTUKa1 (TTUKa2) at the tower.

Unique scanning strategies were employed with the TTUKa systems for varying atmospheric conditions. Altogether, data from 17 time periods with different atmospheric conditions could be recorded: 5 in precipitation and 12 in clear-air environments. The dual-Doppler datasets ranged from 30 min to 7 h, with an average duration of 3 h. Dual-Doppler PPI sectors, ranging from 20° to 60° in width, were performed at multiple elevation angles to provide 3D volume information useful for dual-Doppler synthesis over the domain as in Hirth et al. (2015). Intersecting range–height indicator (RHI) scans provided dual-Doppler radar virtual towers (Gunter et al. 2015) near the tower and the LSS. During precipitation, the dual-Doppler virtual tower was placed directly over the LSS (Fig. 1) with the profile revisit time between 1 and 2 s. However, ground clutter contamination in clear-air scanning environments required that the dual-Doppler profile location (the RHI intersection

point) be shifted away from the strong signal of the tower, approximately 109 m to the southeast of the lidar supersite; ground clutter also required a slower scan speed to amplify the atmospheric signal. RHIs were generally limited to less than 20° in elevation. To compare the TTUKa radars, the BAO tower anemometers, and the scanning lidar measurements during a portion of the project, a “stare” technique was used in which both radars focused on a single azimuth and elevation near the tower at a sampling rate of 5 Hz.

Radiosonde launches. To extend measurements above the BAO tower, approximately 65 Vaisala RS92 radiosondes were launched during XPIA, nominally at 0800, 1200, 1600, and 2000 local time (1400, 1800, 2200, and 0200 UTC) (supplemental material, Table ES1). Forty soundings were launched from the BAO Visitor's Center, while 25 soundings were launched from the Water Tank (see Fig. 1). Temperature and moisture profiles from the soundings are used to evaluate microwave radiometers.

Microwave radiometers and radio acoustic sounding systems. Microwave radiometers (MWRs) provide automated, regular measurements of temperature and moisture structure up to 10 km in the atmosphere (Ware et al. 2003; Bianco et al. 2005; Cimini et al. 2011; Friedrich et al. 2012). These instruments observe atmospheric brightness temperature and apply radiative transfer equations and neural network retrievals in order to estimate profiles of temperature, liquid water, and humidity, as well as integrated water vapor and cloud liquid water path. These retrievals use historical soundings (Ware et al. 2013) as a basis: standard soundings launched from the Denver International Airport, approximately 35 km southeast of the BAO, provided the historical sounding basis. Radiometer vertical retrieval intervals are 50 m from the surface to 500 m AGL, 100-m intervals from 500 m to 2 km, and 250-m intervals from 2 to 10 km.

Two Radiometrics MWR-3000A systems, operated by NOAA and the University of Colorado Boulder, were deployed side by side at the BAO Visitor's Center (Fig. 1). Temperatures observed in the K band (22–30 GHz) and in the V band (51–59 GHz) at zenith and 75° off zenith at 1-min resolution were compared to the six levels of temperature measurements on the BAO tower as well as to temperature profiles from the soundings. Furthermore, radio acoustic sounding systems (RASS) are routinely used to remotely measure vertical profiles of virtual temperature (May et al. 1989); two of these instruments (a NOAA 915- and 449-MHz RASS) were collocated with the MWRs.

MOTION PLATFORM

The XPIA campaign included a study of a controlled “floating lidar,” a technique that uses a Doppler wind lidar to measure the marine boundary layer wind profile on a moving platform, such as a buoy or ship. Interest in floating lidar for wind energy resource assessment is growing as a result of the prohibitive cost of offshore meteorological towers (Archer et al. 2014). Because Doppler lidar measures the wind as relative velocity with respect to the laser source, floating lidar must compensate for platform motion, either by correcting wind data using a high-precision 6-degree-of-freedom (DOF) inertial measurement unit (IMU) or by mechanical stabilization (Pichugina et al. 2012). During XPIA, we compared wind data measurements from two lidars separated by less than 2 m: one mounted on a motion platform and the other at rest. We also compare these data to nearby tower measurements. A similar experiment was recently performed on the coast of Norway (Mathisen 2013).

The UMBC motion platform (patent pending) is a Stewart platform that uses six linear positioners to obtain 6 degrees of freedom of motion: three rotational (roll, pitch, and yaw) and three translational directions (Dasgupta and Mruthyunjayab 2000). The platform, seen in Fig. SBI, is pneumatically driven, controlled by a Beaglebone Black micro-computer (<http://beagleboard.org/BLACK>), and capable of positioning a 300-lb (136 kg) load with vertical velocities up to 0.5 m s^{-1} . Positioning of the platform is accomplished via closed-loop control of each cylinder with its



FIG. SBI. The UMBC pneumatic Stewart platform at the BAO with a Vindicator III mounted. The guy cables of the BAO can be seen in the background.

attached length sensor. The six cylinder lengths uniquely determine the 6 DOF of the platform. Control algorithms are used to prescribe a suite of motion sequences, and actual sea surface motion data can be input for realistic simulations of sea surface motion. A 6-DOF

accelerometer collects motion data while the platform is moving to verify the motion derived from length sensors on each of the six cylinders. The examples shown here highlight instances where changes in the platform motion coincided with changes in wind regime.

Surface flux stations. Three surface flux stations assessed the surface energy balance for XPIA. They are described in the supplemental material and are mentioned here simply to highlight the breadth of the dataset for providing surface flux and surface temperature data for modeling studies. NCAR’s Earth Observing Laboratory deployed two surface stations; each was instrumented to measure all terms of the surface energy balance, using the same types of sensors. The third station, a long-term flux station established in April 2011, is located 91 m west of the BAO tower.

Other wind-profiling instruments. During XPIA, two research wind-profiling radars (WPRs) with RASS capabilities developed by NOAA/ESRL/Physical Sciences Division (PSD) were deployed at the BAO Visitor’s Center, operating at 915 and 449 MHz. Their purpose was to measure vertical profiles of wind speed and direction through the lower troposphere, vertical temperature profiles, depths of the convective boundary layer, and to test new techniques for measuring vertical profiles of turbulence dissipation rate (see “Turbulence dissipation rates from wind-profiling radars”). In

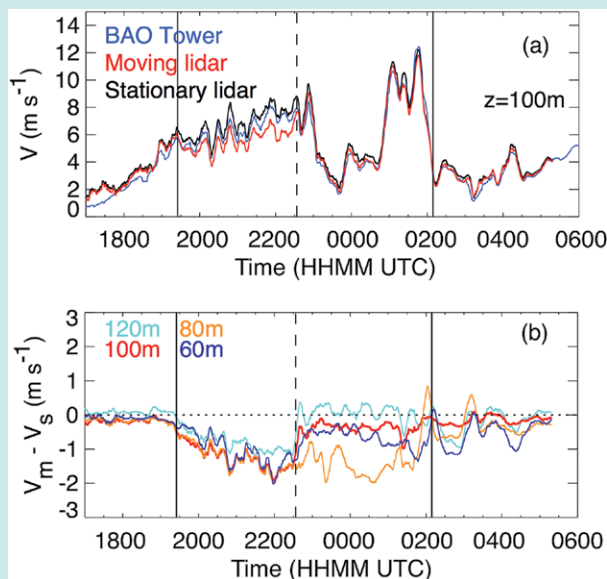


FIG. SB2. (a) Comparison of 100-m wind time series from moving (red) and stationary (black) Vindicator III wind lidars and BAO tower sonic anemometer (blue) data for a 12-h period during XPIA. (b) Difference between the moving and stationary lidar winds at heights 60, 80, 100, and 120 m. The platform was moving from 1924:57 UTC 14 May (~hour 2.5) to 0209:10 UTC 15 May (~hour 9.3) marked by the solid vertical lines; the dashed vertical line marks the time when the motion sequence was changed. All data have been boxcar smoothed with a 10-min window.

First, we compare wind speed measurements from two AXYS Vindicator III lidars: one mounted on the motion platform and the other at rest less than 2 m away. The 100-m-level wind measurements from the two lidars and the tower sonic anemometer were compared for a 12-h period beginning at 1924 UTC 14 May (Fig. SB2). The platform performed periodic roll-

and-pitch rotations at a frequency of 0.15 Hz, corresponding to a dominant wave period of about 7 s, representative of waves in the mid-Atlantic. The platform moved only during the interval bounded by the solid vertical lines (1930 and 0215 UTC in Fig. SB2); the dashed vertical line (2230 UTC) marks the time when the axis of rotation was changed. The motion in the earlier

interval before the dashed vertical line in Fig. SB2 was a 15° amplitude roll, and the motion to the right of the dashed line was a 15° pitch. Both motions were off vertical by about 3° . Note that substantial changes in 100-m winds also occurred during the platform motion experiment.

The differences between the moving and stationary lidar wind speed at heights of 60, 80, 100, and 120 m appear in Fig. SB2b. During the first motion segment, the moving lidar wind speed decreased relative to the stationary lidar by up to 1.5 m s^{-1} , which is likely due to the off-vertical orientation of the platform in combination with the observed increase in wind shear during this time so that lower wind speeds are being sampled by the moving lidar. The wind speed differences decrease during the second segment, despite the rapid increase in wind shear near 0100 UTC. Wind speed differences were largest at 80 m, which may be related to the fact that the stationary lidar reported a wind speed maximum near 100 m that was being sampled by the tilted moving lidar. The differences in the lidars near the end of the motion period and thereafter coincided with a substantial drop in the signal and a change in wind direction that likely brought in a cleaner air mass.

The WCv2 lidar was also mounted on the platform during XPIA to evaluate its internal motion-compensation algorithm, and a comparison of the winds with and without motion compensation for two different motion sequences appears in Fig. SB3. The roll-and-pitch time series (Fig. SB3, bottom) illustrates ►

addition, a wind-profiling Doppler sodar (Atmospheric Systems Corporation) was located at the BAO as part of a longer-term deployment, and a monostatic sodar operated by NOAA provided high-temporal-resolution measurements of the depth of the turbulent boundary layer and gravity wave characteristics.

DATA AVAILABILITY. Each type of remote sensing instrument has limitations regarding atmospheric conditions in which it can collect data. Lidars that operate in the infrared require an atmosphere with

sufficient loading of aerosol particles to act as scatterers and cannot collect data in very clean-air conditions (Aitken et al. 2012) or in heavy precipitation events. On the other hand, Ka-band radars generally perform well during light to moderate precipitation and can collect signal during some but not all clear-air conditions. Therefore, intercomparisons are challenging because of the almost mutually exclusive atmospheric conditions in which the lidar and radar systems operate at their best. Sonic anemometers tend to provide spurious results during precipitation

MOTION PLATFORM, CONTINUED

the motion of the platform. Shaded regions in Fig. SB3 (top) indicate the plus-or-minus one standard deviation bounds of the 1-s wind speed fluctuations about the 1-min mean. The black line shows the wind speeds from the BAO SE sonic anemometer; winds varied from northeasterly to southeasterly, suggesting that the SE anemometer was not waked. Differences in the 1-min means with and without motion compensation are less than 0.25 m s^{-1} (Fig. SB3, middle). However, the effect of motion compensation on variances must be considered for measurements of turbulence intensity, as seen by the variability in the shaded regions of Fig. SB3 (top). Experiments of this type may therefore be useful in assessing uncertainties in lidar measurements of turbulent winds over rough seas.

Two main sources of uncertainty influence the wind profiles measured from a Doppler lidar on a moving platform. First, the motion itself contributes to the Doppler shift and thus alters the line-of-sight wind speed, but this uncertainty can be corrected with a motion-compensation algorithm. Second, the volume of space sampled by the lidar varies with the motion. The latter leads to large uncertainties during inhomogeneous wind conditions. Other findings during the XPIA motion platform experiments included observations of variability in the Vindicator III signal-to-noise (SNR) ratio that were clearly linked to the platform

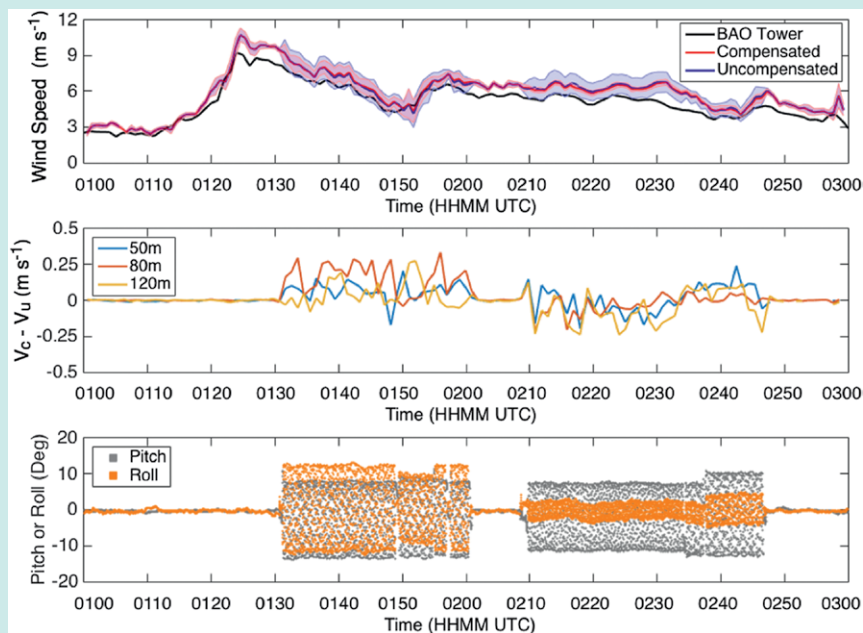


FIG. SB3. Data from 28 May v2 motion-compensation tests: (top) time series of the v2 100-m wind speed with (red) and without (blue) motion compensation and BAO SE sonic anemometer (black). Solid lines are 1-min means, shading indicates the plus-or-minus one standard deviation bounds of the 1-s fluctuations relative to the 1-min mean. (middle) Difference between compensated and uncompensated winds at three heights. (bottom) Times series of pitch (gray) and roll (orange) from the motion table.

motion. For these cases, strong vertical gradients in aerosol loading coupled with intermittent off-vertical scanning resulted in strong variations in optical pathlength—a result that has implications for measurement quality control based on SNR filtering. These types of uncertainties cannot be corrected with a motion-compensation algorithm.

During XPIA, changes in the wind regime sometimes coincided with variations in the platform motion or

orientation, leading to unexpected opportunities to investigate the impact of spatial inhomogeneity on the measured wind profile and other insights. While the platform was designed to simulate sea surface motion, during XPIA its usefulness as a flexible and adaptive platform for remote sensing instruments became apparent. A more comprehensive analysis will appear in a future report.

events (www.campbellsci.com/csats3), and instruments mounted on towers may be affected by tower vibration and/or tower waking (Cermak and Horn 1968; Orlando et al. 2011).

While the instruments all suffered from periodic data outages throughout XPIA, a considerable quantity of data was collected. The TTU Ka-band radars executed test scans each of the 32 days they were on site; environmental conditions warranted further data collection on 17 of these 32 days. The two NOAA 200S systems collected data more than 82% of the time.

The UTD lidar was deployed from 3 March to 1 May (1,412 h) and collected data for 875.2 h (62%), with variable range during this time period. Two of the three WINDCUBE profiling lidars reported data at least 90% of the time during which they were deployed for heights between 40 and 120 m. The AXYS Vindicator III unit 3013 reported greater than 60% availability in the lowest four range gates (55, 60, 80, and 100 m AGL), whereas the percent of data available for unit 3015 only slightly exceeds 50% at 80 and 100 m AGL as a result of lower signal strength. Microwave radiometers

TABLE 1. Doppler lidar locations and period of deployment during the XPIA field campaign.

Instrument	Location	Latitude	Longitude	Elevation (m)	Start date	End date
HRDL (NOAA)	Water Tank	40.0409°N	104.99845°W	1,602	5 Mar	5 May
Dalek 1 (NOAA)	Visitor's Center	40.04533333°N	105.005717°W	1,587	2 Mar	9 Mar
	Erie High School	40.04701667°N	105.01625°W	1,582	9 Mar	26 Apr
	Visitor's Center	40.045366°N	105.005669°W	1,587	26 Apr	1 Jun
Dalek 2 (NOAA)	Visitor's Center	40.04533333°N	105.005717°W	1,587	6 Mar	1 Jun
UTD lidar	Visitor's Center	40.045346°N	105.005751°W	1,587	3 Mar	6 Mar
	NE Pad	40.05063333°N	105.001133°W	1,582	6 Mar	27 Apr
	Visitor's Center	40.045346°N	105.005751°W	1,587	27 Apr	1 May
UMBC lidar	Water Tank	40.040811°N	104.998595°W	1,602	10 Apr	16 Apr
	NW Pad	40.050696°N	105.005243°W	1,578	16 Apr	28 Apr
	Visitor's Center	40.045346°N	105.005751°W	1,587	28 Apr	2 May

collected temperature and moisture profiles every day except during precipitation or power outages.

SCANNING LIDAR RETRIEVALS OF WIND PROFILES.

The XPIA lidar scanning strategies were designed to extract quantitative information about different aspects of the atmospheric boundary layer velocity field (Mann et al. 2008; Sathe and Mann 2013; Banta et al. 2015) with one or with more lidars. Holding the lidar beam stationary (also known as a stare) results in a range versus time dataset and allows assessment of single-component mean flow and turbulence statistics (Banta et al. 2002, 2006; Pichugina et al. 2008; Iungo et al. 2013). Three-dimensional fixed-point measurements were performed by synthesizing the radial velocities measured simultaneously by three or more lidars intersecting at a fixed position (Newsom et al. 2008; Hill et al. 2010; Vasiljević 2014; Carbajo Fuertes et al. 2014; Berg et al. 2015). Note that our multiple-lidar coordinated scans were performed by syncing all lidars to a common time server and triggering the scans at a given server time. The scan start delay and scanner slew delay were taken into account to ensure maximum coordination rather than via an integrated software or hardware interface as has been demonstrated with the WindScanner system (Vasiljević 2014; Berg et al. 2015). Turbulence statistics such as the momentum flux can also be evaluated through multiple scanning lidars (Sathe et al. 2011). Below, we discuss the accuracies of the different scanning strategies as compared to conventional instruments.

Scanning lidar line-of-sight velocity evaluation with tower anemometry. We first assessed the measurement accuracy of the three 200S Doppler lidars (Dalek 1, Dalek 2,

and UTD lidar) by comparing the LOS measurements from the three 200S lidars to sonic anemometer measurements. This procedure allows for a direct evaluation of Doppler lidar radial velocity measurements. Approximately 345 h of stare scans throughout XPIA were targeted at the tower sonics; all such data over the period of the deployment are included here. The sonic-measured LOS velocity V_r is evaluated by considering the lidar orientation toward the sonic, quantified with the azimuth (θ) and elevation (ϕ) angles from the lidar toward the sonic. Here, u , v , and w are the sonic measurements along the west–east, south–north, and vertical axes, respectively:

$$V_r = u \sin \theta \cos \phi + v \cos \theta \cos \phi + w \sin \phi. \quad (1)$$

Correlation coefficients between the lidar LOS and the sonic LOS wind speeds are close to 1 for all three systems (Figs. 2a,c,e). Dalek 1 and Dalek 2 show no significant bias in the LOS measurement (Figs. 2b,d), while there is a bias of 0.6 m s^{-1} for the UTD lidar (Fig. 2f). Later analysis determined that this bias, due to improper calibration of the “frequency chirp” in the laser pulse, was stable and reproducible in several tests independent of the sonic anemometer comparison presented here, and could simply be subtracted out of the UTD lidar measurements. This experience underscores the importance of calibration of these instruments in the field—if a local tower is not available, then long-term vertical velocity stares or comparisons with other instruments (Vanderwende et al. 2015) can be used to identify potential biases.

Scanning lidar virtual tower of 3D winds: Evaluation with tower anemometry. The virtual tower technique can define profiles of winds and turbulence at multiple

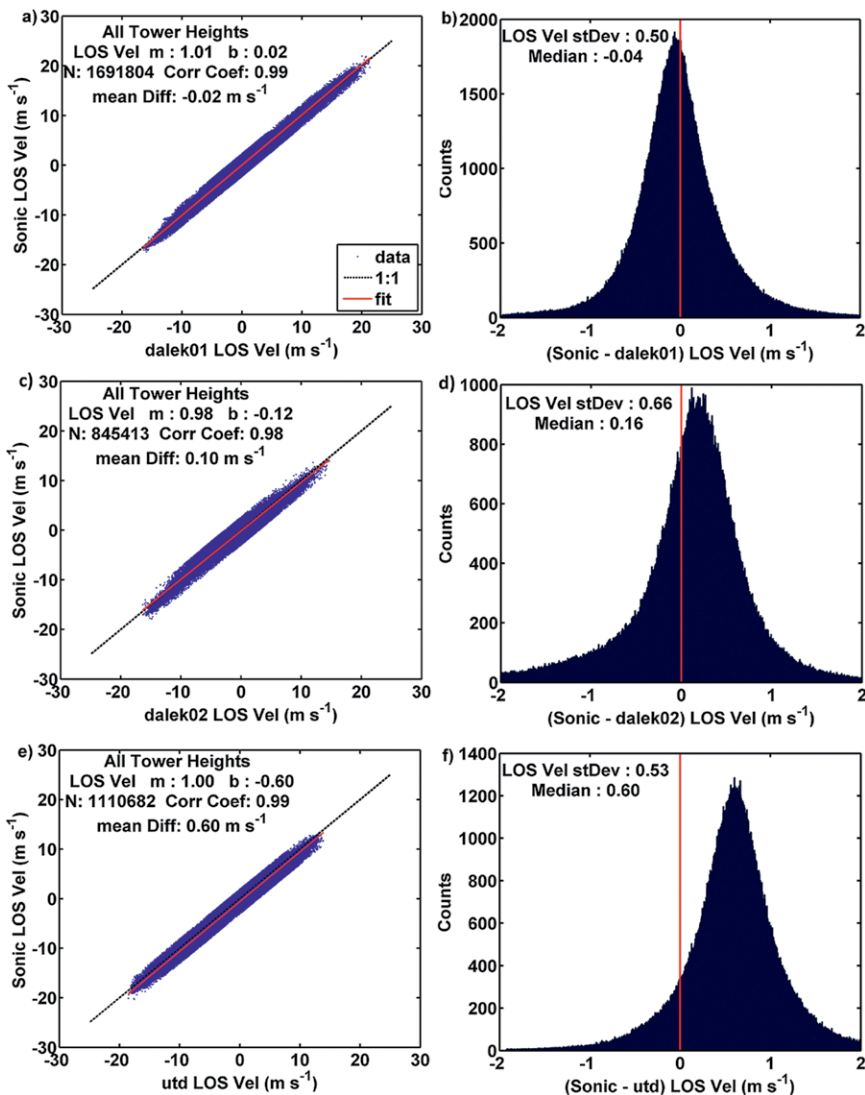


FIG. 2. Comparison of the 200S instantaneous LOS measurements to I-s averaged sonic-derived LOS measurements at all levels on the BAO tower for all available times. (a) Comparison of Dalek 1 LOS measurements with sonic LOS measurements. (b) Distribution of difference between Dalek 1 LOS and sonic LOS. (c) Comparison of Dalek 2-measured LOS with sonic LOS measurement. (d) Distribution of difference between Dalek 2 LOS and sonic LOS. (e) Comparison of UTD lidar LOS measurement with sonic LOS measurement. (f) Distribution of difference between UTD lidar LOS and sonic LOS.

locations within a wind farm, enabling investigators to move locations of measurements as the wind direction changes. During XPIA, we evaluated a measurement strategy for creating virtual towers of the three components of the wind field using triple-Doppler stars. Three 200S lidars stared simultaneously at a common volume near the southeast sonic anemometers on the BAO tower for 25 s at each of the six levels (Fig. 3). To retrieve the three components of the wind, all LOS measurements within a volume (35 m × 35 m in the horizontal, 15 m in vertical, and 15 s in time)

Doppler virtual towers (previous subsection) were also compared to those from the TTU Ka-band radars, with a goal to understand not only how the retrievals compared, but also to study the effect of temporal and spatial averaging. With this in mind, triple-Doppler virtual tower data were processed in two ways: 1) instantaneous retrieval, where the retrieval was made using one 500-ms accumulation time LOS measurement from each lidar in Eq. (1) and 2) 25-s accumulation retrieval, where 25 s of LOS measurements were used to retrieve the wind field using Eq. (1).

were collected and fit to Eq. (1), using least squares, to solve for u , v , and w .

These estimates compare well with the sonic anemometer measurements at all levels (50–300 m), with correlation coefficients of 0.97 (0.99) for wind speed (direction), slopes near 1, and very small offsets (Figs. 4a–d). Vertical velocity estimates are compared only to sonic anemometers at 150 m or higher (Figs. 4e,f): vertical velocity retrievals were noisy at the 50- and 100-m levels because of the low-elevation angles. In contrast, higher-elevation scans show agreement between retrieved velocities and sonic anemometer estimates with a slope close to 1 and minimal offset but a lower correlation coefficient of 0.86 (Figs. 4e,f). We find the virtual tower approach to be reliable for estimates of horizontal wind speed and wind direction, with greater uncertainty for vertical velocity estimates especially at low-elevation angles.

Scanning lidar virtual tower of 3D winds: Comparison to dual-Doppler Ka-band radar retrievals. Horizontal wind field retrievals from triple-

TURBULENCE DISSIPATION RATES FROM WIND-PROFILING RADARS

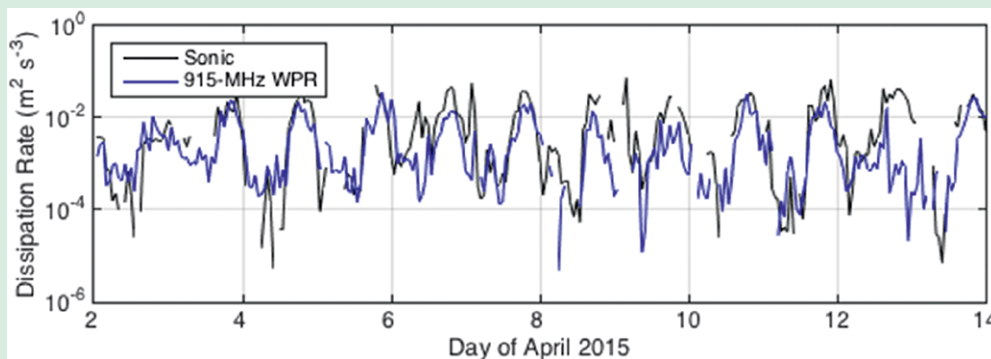
Radar wind profilers are widely deployed, typically providing profiles of mean wind speed and direction in the lowest 2–8 km of the atmosphere. If these instruments could provide turbulence metrics such as dissipation rate, a vast new dataset could be used for improving turbulence parameterizations in numerical weather prediction models. During XPIA, wind-profiling radars at the Visitor Center (Fig. 1) were used to measure turbulence dissipation rates, improving upon results obtained using the method introduced by Hocking (1985) that relates the width of the Doppler velocity spectrum to the dissipation rate. The 915-MHz radar ran in “turbulence optimized” mode (McCaffrey et al. 2016a) for 30 min of each hour, in a vertically pointed beam mode at 25-m vertical resolution. Short dwells of 15 s were used, and time series were saved for more detailed postprocessing. The processing method is as follows: filtering the time series through Wavelet and Gabor

methods (Jordan et al. 1997; Lehmann and Teschke 2008; Bianco et al. 2013); computing the fast Fourier transform (FFT) to obtain the Doppler spectrum for each dwell; removing ground clutter and interference, and averaging 2 min (eight dwells) of Doppler spectra to accurately capture turbulent time scales; calculating the first and second spectral moments using the standard peak processing method (not the multiple peak processing method used for mean winds); and finally computing the turbulence dissipation rates based on the spectral width and radar properties, such as beam-broadening angles. High spectral resolution determined by the optimized radar setup and number of points used in the FFT allowed widths to be calculated well below the sizes previously observed by WPRs (Jacoby-Koaly et al. 2002), enabling the smallest dissipation rates to be captured.

Over 12 days, this method shows strong agreement with the traditional

inertial dissipation method using data from the tower sonic anemometers (Fig. SB4). The dissipation rates from the sonic anemometers are hourly averages of the 15-min values obtained through the inertial range technique in the mean wind direction, using $\alpha = 0.52$, and averaged over sonics on opposite sides of the tower (except when one was waked). The diurnal cycle in turbulence appears, with dissipation rate values peaking in the daytime convective boundary layer and decreasing by two orders of magnitude during stable nighttime conditions. This agreement with the in situ measurements encourages further use of radar wind profilers, normally only used for first-moment (mean) winds, for observing turbulence profiles. With 25-m resolution in the lowest 1–2 km of the boundary layer, turbulence characteristics from wind-profiling radars will provide new and extensive information for improving turbulence parameterizations in numerical weather prediction models.

FIG. SB4. ▶ Hourly average turbulence dissipation rates as measured at 100 m by the sonic anemometers (black) and the 915-MHz wind-profiling radar (blue) over 12 days from 2 to 13 Apr 2015.



This analysis used data from 1320 to 1507 UTC 25 March during neutrally-stratified conditions with light winds and overcast skies: the Ka-band radars had good signal availability and performed RHI scans intersecting at the LSS to create “virtual tower” profiles of wind speed and direction. Each Ka-band RHI scan took 3.3 s on average. Dual-Doppler wind speed and direction profiles were then created from each pair of RHI scans. The three 200S lidars scanned as described in the previous subsection.

The lidar and radar retrievals sample slightly different time periods, but their comparison is instructive. Each lidar retrieval, whether instantaneous or 25-s accumulated, was compared with the nearest (in time) radar retrieval, as well as to 1-Hz WCv2 measurements. Figure 5 shows the comparison at 120 m AGL. The mean and median of the instantaneous retrievals from the triple-Doppler reconstruction agree well with the WCv2 and Ka-band dual-Doppler retrievals. However, the 25-s retrieval does not always

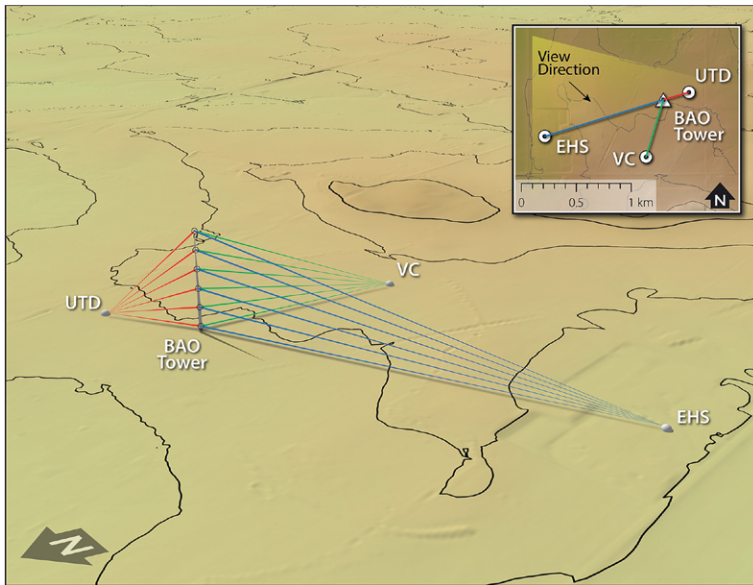


FIG. 3. Schematic of the virtual tower stares study. The three 200S systems stared at a location just south of the southeast sonic anemometers on the BAO tower for 25 s at each level to create a virtual tower of 3D wind fields.

agree (especially at other heights) with the instantaneous retrievals, indicating these two methods of deriving the wind field are not equivalent. Further analysis is required to specify the conditions when these two methods are equivalent.

The 25-s accumulation retrievals do agree with the Ka-band dual-Doppler retrievals (Fig. 6) for horizontal wind speed ($R^2 = 0.93$) and wind direction ($R^2 = 0.95$). The 25-s accumulation seems to remediate much of the variation observed in the instantaneous retrieval.

Scanning lidar coplanar scans of 3D winds: Evaluation with tower anemometry. To enable more rapid vertical profiling than possible with coordinated stares, XPIA tested an approach in which each lidar executed a “vertical slice” or RHI scan, with the intersection line at the lidar supersite for heights between 60 and 200 m (0300–0400 UTC 21 April). The UTD lidar scanned toward Dalek 1, while Dalek 1 scanned toward the UTD 200S lidar and Dalek 2 measured orthogonally to the RHI plane determined by the other two lidars, similar to the scenario of Fig. 3 but with a continuous sweep rather than pauses at the levels of the sonic anemometers. The in-plane (along the Dalek 1–UTD line) and transverse velocity components were retrieved from the radial velocities measured by Dalek 1 and the UTD lidar. Their vertical velocity was then combined with the radial velocity of Dalek 2 to calculate the transverse velocity. More details on this test can be found in Debnath et al. (2016). The

two horizontal velocity components exhibit correlations between 0.85 and 0.66, compared with the data acquired from a profiling lidar (Fig. 7). The retrievals of the vertical velocity exhibit large errors, possibly owing to the difference in the measurement volumes, the challenge of distinguishing the small vertical velocity signal, or the shallow scanning elevation angle. This large error also suggests that triple-lidar retrievals of vertical velocities are vulnerable to significant errors, at least for lidar orientations similar to those used in XPIA.

SCANNING RADAR RETRIEVALS OF WINDS.

The TTU Ka-band radar team collected multiple virtual tower datasets, with atmospheric conditions dictating the radar scan parameters. Nonprecipitating environments sometimes required

slightly slower scan speeds to preserve data quality, resulting in a range of scan rates of 5° – $30^{\circ} \text{ s}^{-1}$. After single-Doppler RHI quality-control procedures removed ground clutter, regions of poor data quality, and second-trip echoes, the single-Doppler radial velocities at the intersection location were averaged into bins with a 20-m vertical resolution, typically between 10 and 500 m AGL. The binned data from each radar were then synthesized to determine the horizontal velocity at multiple levels of the RHI intersection point as in Gunter et al. (2015).

During a clear-air dataset from 16 March 2015, the RHI intersection location was ~ 200 m southeast of the BAO tower, and the time to complete a profile varied between 4.97 and 16.3 s (from 6° to $1.5^{\circ} \text{ s}^{-1}$). Four time periods exhibiting good data quality and large wind speed variability were selected for the dual-Doppler analysis. Both the dual-Doppler retrieval and the 150-m BAO tower sonic anemometers captured the wind speed ramp and evolving wind direction (Fig. 8) associated with the passage of a boundary that resembled a density current in the TTUKa RHI scans (not shown). Mean wind speed profiles during this time demonstrated excellent agreement. Wind directions from the SE sonic anemometers and the dual-Doppler method agree within 1° below 250 m, while the NW sonic anemometers exhibit a southerly bias, perhaps because of flow deflection around the tower (Fig. 8) despite the fact that neither the NW or SE booms were shadowed directly by the tower during

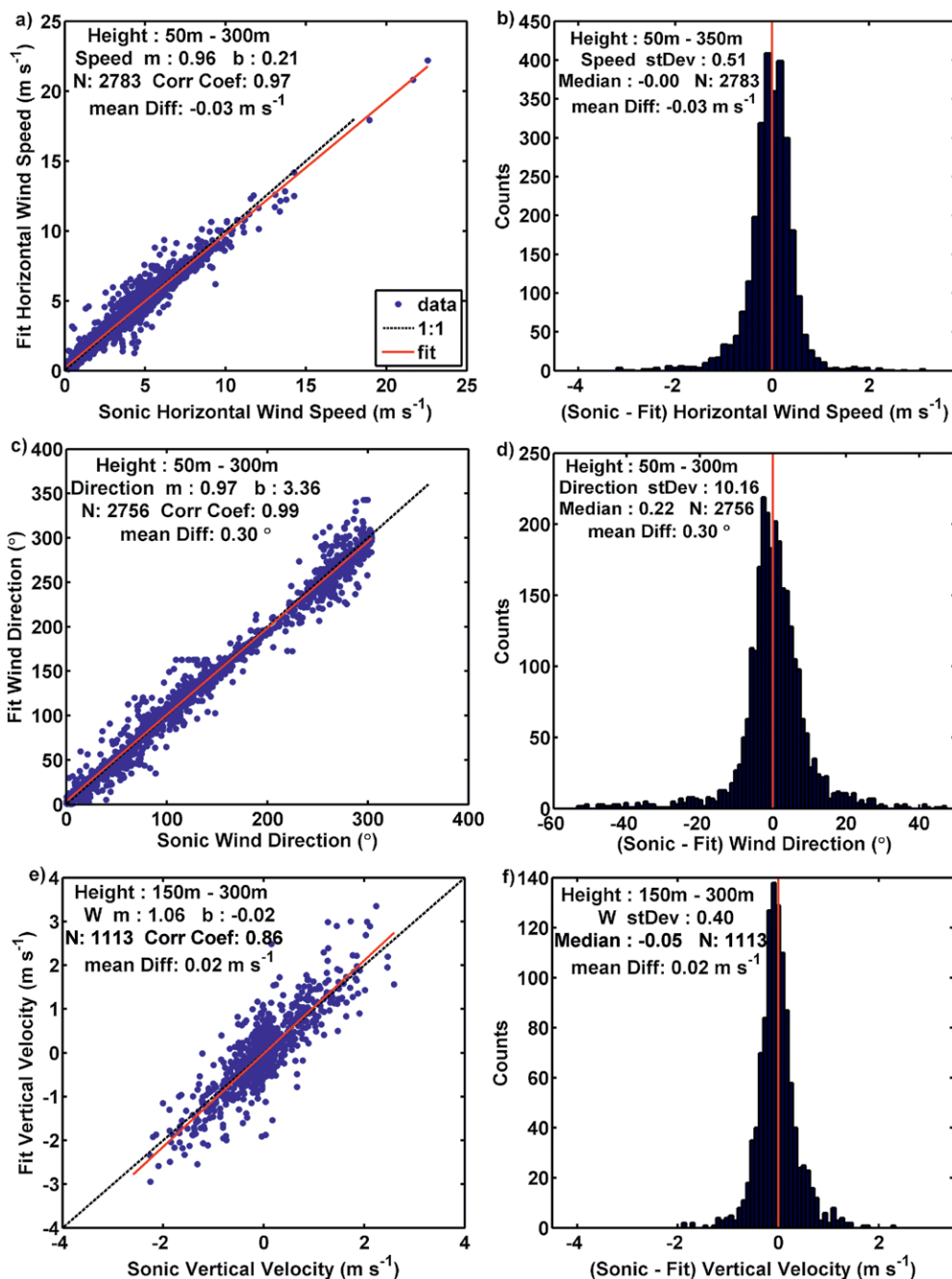


FIG. 4. Comparison of 3D wind retrievals from triple-Doppler virtual tower stares with 15-s filtered sonic measurements. (a) Comparison of horizontal wind speed from triple Doppler with sonic measurement at all levels. (b) Histogram of difference between horizontal wind speed retrieval from triple Doppler and sonic measurement. (c) Comparison of horizontal wind direction from triple Doppler with sonic measurement at all levels. (d) Histogram of difference between horizontal wind direction from triple Doppler and sonic measurement. (e) Comparison of vertical velocity from triple Doppler with sonic measurement at levels 150–300 m. (f) Histogram of difference between vertical velocity from triple Doppler and sonic measurement.

these northeasterly flows (McCaffrey et al. 2016b). The other three time periods show similar agreement.

Dual-Doppler winds can be compared to the sonic anemometer winds at the nearest level. The correlation coefficients computed between the

dual-Doppler and sonic anemometer winds increased with height (Fig. 9) and exceeded 0.90 for most levels despite the horizontal separation of approximately 200 m between the tower and the dual-Doppler profile location.

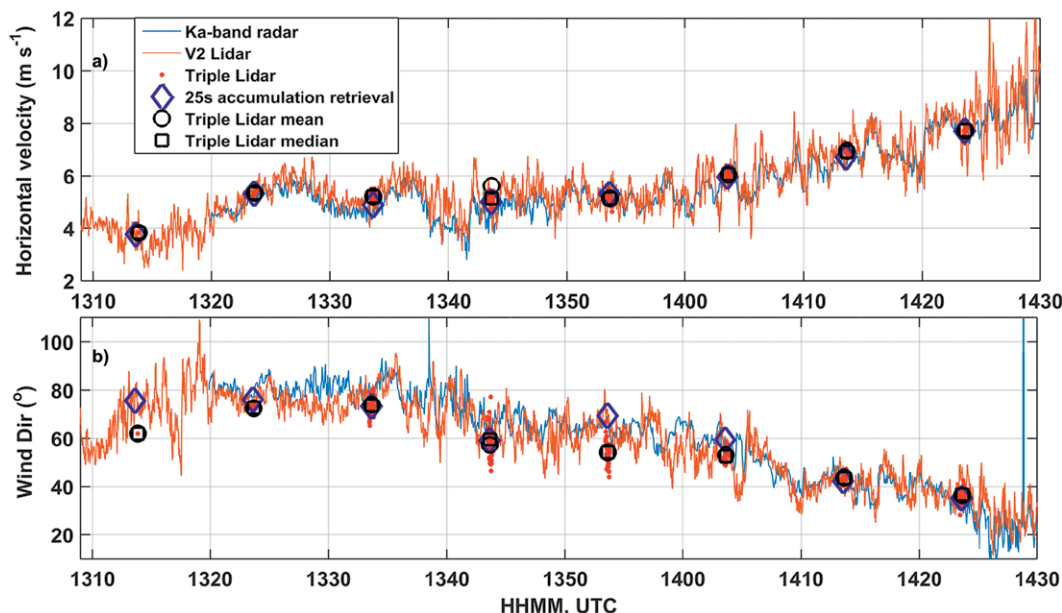


FIG. 5. Comparison of (a) wind speed and (b) wind direction derived from different techniques and platforms at 120 m AGL at the lidar supersite location on 25 Mar showing the effect of spatial and temporal averaging on the wind field retrieval.

Bias for the 16 March dataset was also investigated by computing the composite wind speed and direction profiles for all four periods (Fig. 10). Composite dual-Doppler wind speed profiles displayed little bias ($<1 \text{ m s}^{-1}$) from the sonic anemometer wind speed profiles, but the bias increased with height. Except at the 50-m level, the biases between the dual-Doppler and SE sonic anemometer wind speeds were less than the dual-Doppler-NW sonic anemometer biases at each comparison level. (Note that for a wind direction between 40° and 60° , neither sonic is directly waked.) Wind speed root-mean-square error (RMSE) values were uniform with height and ranged from 1.34 to 1.63 m s^{-1} . The positive bias in the NW sonic anemometer wind direction that was noted in all four separate time periods was also evident in the composite profile, with the mean NW sonic anemometer wind direction exceeding the mean dual-Doppler and SE sonic anemometer wind directions at all heights by a maximum of 8.76° . The dual-Doppler wind direction was only slightly veered compared to the SE sonic anemometer with a maximum positive bias of 5.08° .

COMPARISON OF MULTI-DOPPLER LIDAR VOLUME RETRIEVALS AND DUAL-DOPPLER KA-BAND RADAR RETRIEVALS.

During the XPIA field deployment, several experiments were conducted to coordinate simultaneous multi-Doppler lidar and dual-Doppler Ka-band radar measurements and to compare the respective

retrievals. Of particular interest is the spatial variability in the flow: can triple-Doppler lidar quantify spatial variability similarly to the faster-scanning dual-Doppler radars?

One challenge in retrieving gridded three-component wind fields over large spatial volumes using Doppler lidars is the time required to cover the full volume with continuous scans that overlap in time and space to obtain sufficient LOS statistics to create a triple-Doppler retrieval. This overlap requires that each instrument scan a grid point over a time interval less than what is characteristic of the time evolution of the flow. However, the ability of the systems to move quickly from one grid point to the next is constrained by several factors. First, the data rate of the lidar systems requires multiple seconds spent staring at each grid point to obtain accurate LOS values. Second, the instrument locations affect the ability of each lidar to interrogate each point in the entire volume; lidars positioned close to the sampled volume required the scanning head to traverse a larger angular range than if the lidars were located farther from the volume, hence requiring a longer scanning time per repeat cycle. Further, as we require the lidars to scan each point while overlapping in time, the scanning strategy must ensure enough time is spent on overlapping LOS measurements for a robust wind measurement before moving to the next grid point. For the locations used here, several seconds of “idle” time are included in some of the systems in order to allow other systems to “catch up” to the desired

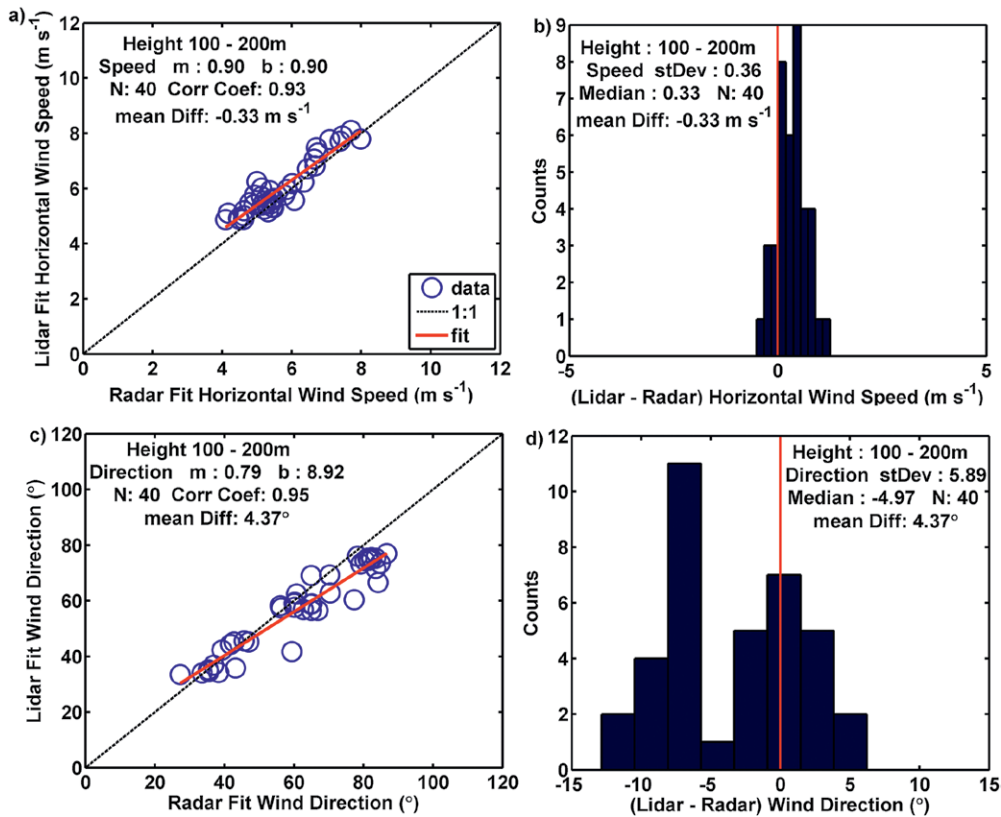


FIG. 6. Comparison of 25-s triple-Doppler lidar with dual-Doppler TTU Ka-band radar retrievals of (a) wind speed, (b) histogram of the difference in wind speed between the triple-Doppler lidar and dual-Doppler radar, (c) wind direction, and (d) histogram of the difference in wind direction during the 1320–1507 UTC 25 Mar period.

grid location. Finally, it is also important to ensure the right mix of azimuth and elevation angle variability in the LOS measurements to have robust horizontal and vertical velocity measurements (Debnath et al. 2016). Therefore, the retrieval update rate, or how often each grid point is revisited by all three instruments simultaneously, has a minimum value for a given deployment setting, scan geometry, and density of grid points. For the XPIA geometry, considering wind speeds between 5 and 10 m s⁻¹, this minimum value would be too large

to capture features before they advected out of the retrieval domain if the domain consisted of contiguous closely spaced grid points. Therefore, to reduce the time required to create a 3D retrieval over a larger volume, we designed a scanning strategy to sample a sparse array of points within the domain of interest, toward developing a sufficient representation of the spatial variability of the flow within that area.

This large checkerboard (LCB) approach was tested during XPIA (Fig. 11). Sixteen points (4 × 4 grid)

at 100 m AGL were sampled sequentially (with a 7-s stare at each location) in a manually coordinated fashion by three 200S scanning Doppler lidars (NOAA Dalek 1, NOAA Dalek 2, and the UTD system) with all three lidars probing a given grid point at overlapping times. The LCB produced this gridded estimate of the horizontal wind field once every 2 min with each

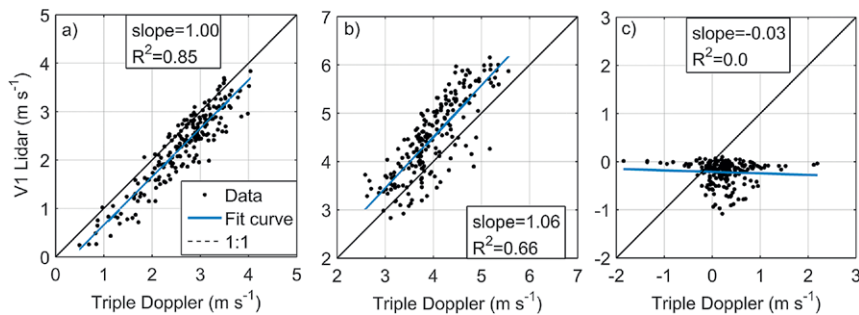


FIG. 7. Wind velocity components retrieved through the lidar coplanar RHI scans and triple-Doppler data analysis and v1 lidar: (a) in-plane velocity, (b) transverse velocity, and (c) vertical velocity for the 0300–0400 UTC 21 Apr period.

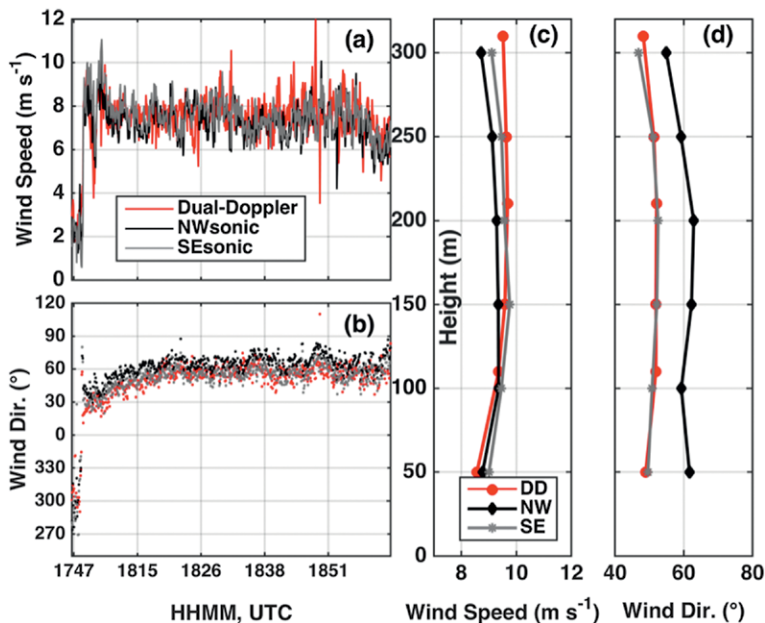


FIG. 8. Dual-Doppler Ka-band radar horizontal (a) wind speed and (b) wind direction time history for the 150-m sonic anemometer and dual-Doppler level and mean profile comparison of (c) wind speed and (d) wind direction for the 1746–1929 UTC period of the 16 Mar 2015 clear-air dataset.

measurement point constructed from radial velocity measurements collected within a 15-s time window (to account for the fact that the lidars were not perfectly coordinated in time). Despite the 144 h of LCB scanning conducted during XPIA, only 20 min of overlap existed between LCB and dual-Doppler Ka-band radar (DDR) retrievals. This lack of coordinated data is partially due to instrument availability (LCB scanning commencing a week before the Ka-band radars departed XPIA) and partially due to the almost mutually exclusive atmospheric conditions in which the two systems operate at their best. (Lidars perform best in clear air, while the radars perform best in light precipitation, although the radars did collect over 5 h of quality clear-air dual-Doppler volumes.)

Nevertheless, the effectiveness of the triple-lidar volume retrieval can be quantified by comparing the LCB retrievals over this 20-min period to DDR retrievals at the same altitude and near the same locations. The DDR retrieved the horizontal wind field every 30 s through a volume of 200×250 horizontal grid points (with a range resolution of 15 m) and 15 vertical grid points (in comparison to the 2 min required for the LCB geometry described above). Agreement between the two systems was determined by calculating, at each of the 16 LCB measurement locations, the difference between the LCB value and the DDR retrieval closest in time and space. The RMSE was 0.39 m s^{-1} (2.81°) with

a correlation of 0.79 (0.71) for wind speed (direction) (Fig. 12). Although this intercomparison dataset is limited, the comparison suggests that these platforms each provide a useful capability for characterizing boundary layer winds. Figure 13 shows wind speed retrievals from six consecutive 2-min LCB planes overlaid on the corresponding DDR retrieval composited over the time taken to complete each LCB plane.

The techniques capture similar spatial variability of the boundary layer during this time period, with “spatial variability” defined as the standard deviation of the wind speed and direction. To determine if the LCB can quantify spatial variability present over a measurement domain, spatial variability estimates from an LCB retrieval (defined as the standard deviation of wind speed or direction over the 4×4 grid points) were compared to the standard deviations from

the DDR retrieval determined over its 200×250 grid points. The spatial variability measured by the LCB and DDR retrievals over a scan interval represents a spatial and temporal convolution that makes comparing the two retrievals nontrivial. Herein, the spatial variability estimate from the LCB is compared to the DDR estimate of spatial variability by calculating the spatial variability over all the DDR planes that fall within the time interval to create that LCB plane (Fig. 14). (Although one approach to quantifying spatial variability from the radars is shown here, other approaches appear in the supplemental material.)

The time series of the spatial variability estimates from the LCB and DDR in Fig. 14 are surrounded by a blue shaded area that shows the measurement difference bounds between the two retrieval techniques, quantified as the RMS difference between the LCB and DDR measurements. The differences could arise because of the following reasons:

- 1) differences in the two instrument’s error characteristics (error in LOS estimate, pointing error, etc.),
- 2) spatial and temporal differences in the sampling of a given grid point between the two sets of instruments, and
- 3) variations in the spatial sampling of the domain of interest (complete sampling for DDR vs sparse sampling for LCB).

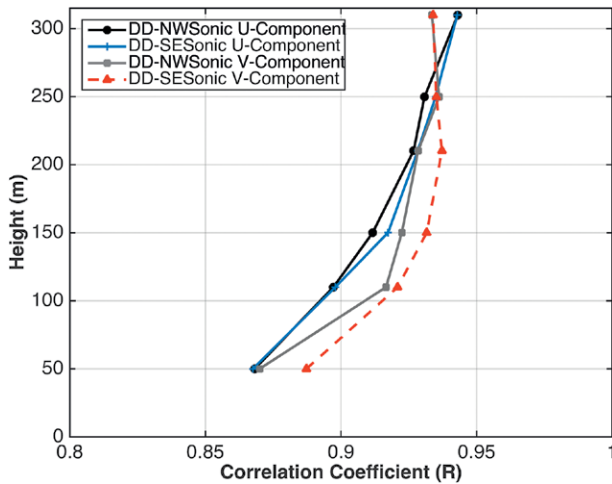


FIG. 9. Correlation coefficients between the dual-Doppler (DD), northwest (NW) sonic anemometer, and southeast (SE) sonic anemometer u and v component winds for the 16 Mar 2015 clear-air dataset. Correlation coefficients were computed based on the four periods of data collected between 1746 UTC 16 Mar and 0216 UTC 17 Mar.

Theoretically, the measurement difference bounds (determined from the RMSE values reported in Fig. 12) should capture the differences arising as a result of points 1 and 2 above. From Fig. 14, we see that in all instances but one, the spatial variability estimates from the two methods are well within these bounds. In addition, the magnitude of the spatial variability estimates is larger than the RMSE differences between the LCB and DDR techniques, indicating that the spatial variability signal is clearly detectable.

Given the very short intercomparison period, it is difficult to make any concrete conclusions from this comparison, but we can try to determine the quality of the comparison made in Fig. 14. The LCB measurement strategy using the current scan geometry and lidar capabilities is well suited to capture lower wind speed cases, which allow sampling a feature several times before it advects out of the domain, but this scan geometry is not suited to high wind speed cases, where a feature may advect out of the domain before it is properly sampled. For example, wind speeds of less than 5 m s^{-1} will allow sampling a feature at all grid points the feature encounters along its way, while a wind speed greater than 16.5 m s^{-1} will allow a feature to be

sampled only once. The mean wind speed during this period was 8.1 m s^{-1} , which is toward the lower end of this spectrum and therefore gives some confidence that the agreement we observe in Fig. 14 has some value. Therefore, given the conditions present in the 15-min period, the LCB technique captures aspects of the spatial variability as observed by the DDR retrievals. To determine how well the LCB technique estimates spatial variability for different wind and stability conditions, in future work this analysis will be extended by using 2D winds retrieved using optimal interpolation (Choukulkar et al. 2012) on PPI scans performed by HRDL during the full 144 h of this experiment. The LCB strategy could be suitable for higher wind speed cases for different volume sizes and scan geometries or when using instruments with faster scan rates.

ASSESSING UNCERTAINTY FOR REMOTE SENSING OF TEMPERATURE STRUCTURE.

Atmospheric stability is known to impact wind turbine wake dynamics (e.g., Högström et al. 1988; Mirocha et al. 2015), wind turbine power performance (Gottschall and Peinke 2008; Wharton and Lundquist 2012; Vanderwende and Lundquist 2012; Dörenkämper et al. 2015), and loads on wind turbine structures (Sathe et al. 2013). To quantify the uncertainty of routine assessments of atmospheric stability, MWR measurements of temperature structure were compared to the six levels of temperature measurements on the BAO tower as well as to temperature profiles from the

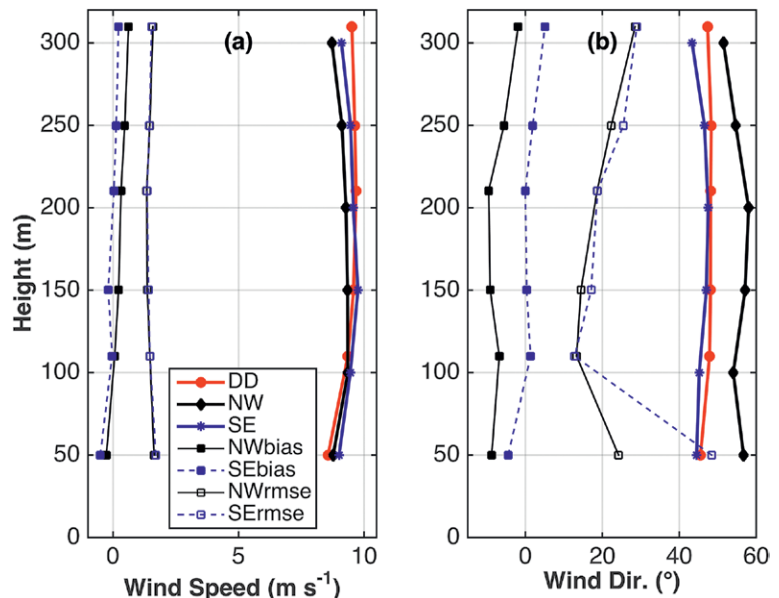


FIG. 10. Composite (a) wind speed and (b) wind direction profiles for 16 Mar 2015 clear-air dataset. The composites are based on the four time periods analyzed between 1746 UTC 16 Mar and 0216 UTC 17 Mar. Bias and RMSE profiles are included.

soundings launched during XPIA. Because the RASS remotely measure vertical profiles of virtual temperature, temperature and humidity profiles from the radiosondes were used to calculate virtual temperature profiles for comparison with the RASS. The volumes sampled by the MWR and RASS systems are substantially larger than those sampled by the soundings or the tower-based temperature measurements. For this reason the analysis uses vertical averaging or linear interpolation when needed, to facilitate comparison.

The coefficient of determination R^2 between the MWRs and soundings for heights up to 1.5 km exceeded 0.98, with mean absolute errors (MAE) near 1.2 K (Fig. 15a). The R^2 values between the RASS and soundings over this same height range were nearly as large (0.97), but the MAE was considerably smaller, averaging 0.7 K (Fig. 15b). With six elevations available for comparison between the radiometers and the tower, R^2 for temperature is 0.99, with an MAE around 0.8 K (Fig. 15c). The RASS–tower comparisons show equally high R^2 (0.99) and a similar MAE of approximately 0.7 K (Fig. 15d).

In summary, the MWR and RASS temperatures show excellent agreement with the soundings and the tower measurements (and thereby with each other), with the RASS providing lower MAE than the MWR above the lowest several hundred meters. Within the first several hundred meters, where the MWR provides its best, highest-resolution data, the RASS and MWR

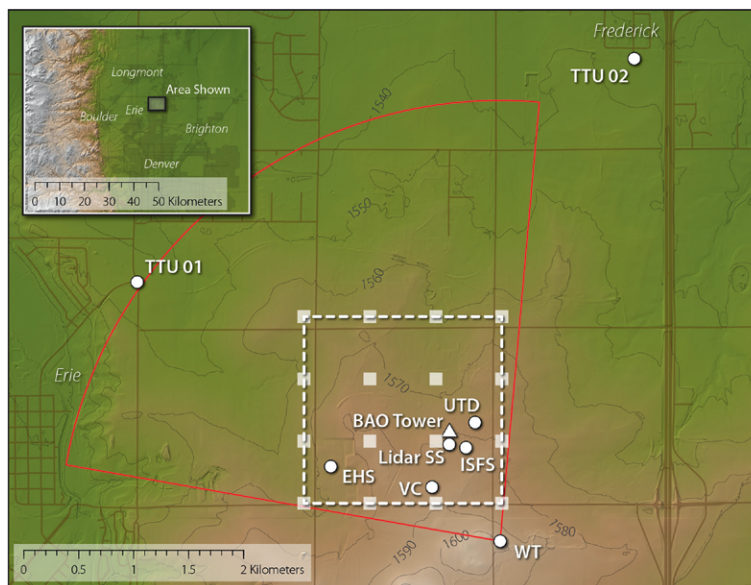


FIG. 11. Layout of the large checkerboard. The gray boxes (not to scale) indicate the overlap locations of the three lidar beams to create a wind retrieval. The red outline shows the coverage of the PPI scan done by HRDL [from the Water Tank (WT)] to envelope the LCB volume.

accuracy are very similar. Because these data were collected throughout the diurnal cycle in a wide range of synoptic weather conditions, we infer the radiometers provide robust and reasonably accurate temperature measurements during most atmospheric conditions. Detailed comparisons, investigated as a function of atmospheric stability, appear in Bianco et al. (2016).

Furthermore, atmospheric lapse rates are often measured from radiometers to assess atmospheric stability conditions, perhaps in conjunction with collocated instruments that provide wind profiles to estimate the Richardson number (Friedrich et al. 2012). The lapse rate measured by the radiometers

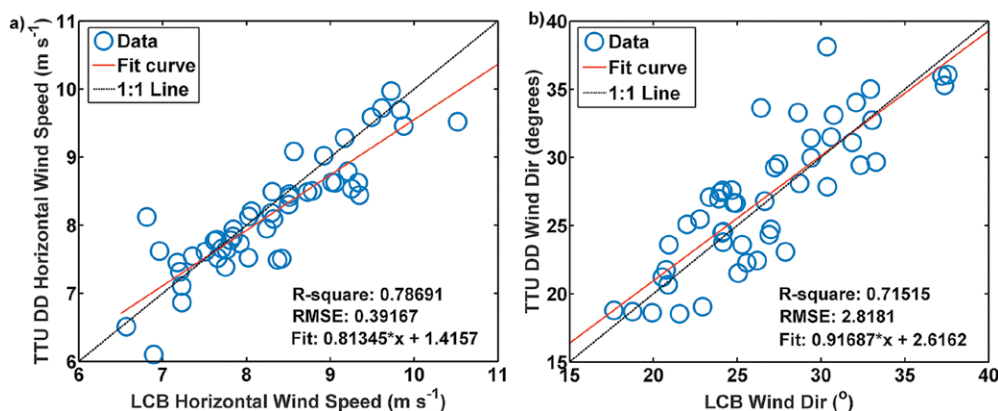


FIG. 12. Comparison of the LCB retrievals with the dual-Doppler radar retrievals: (a) horizontal wind speed and (b) wind direction.

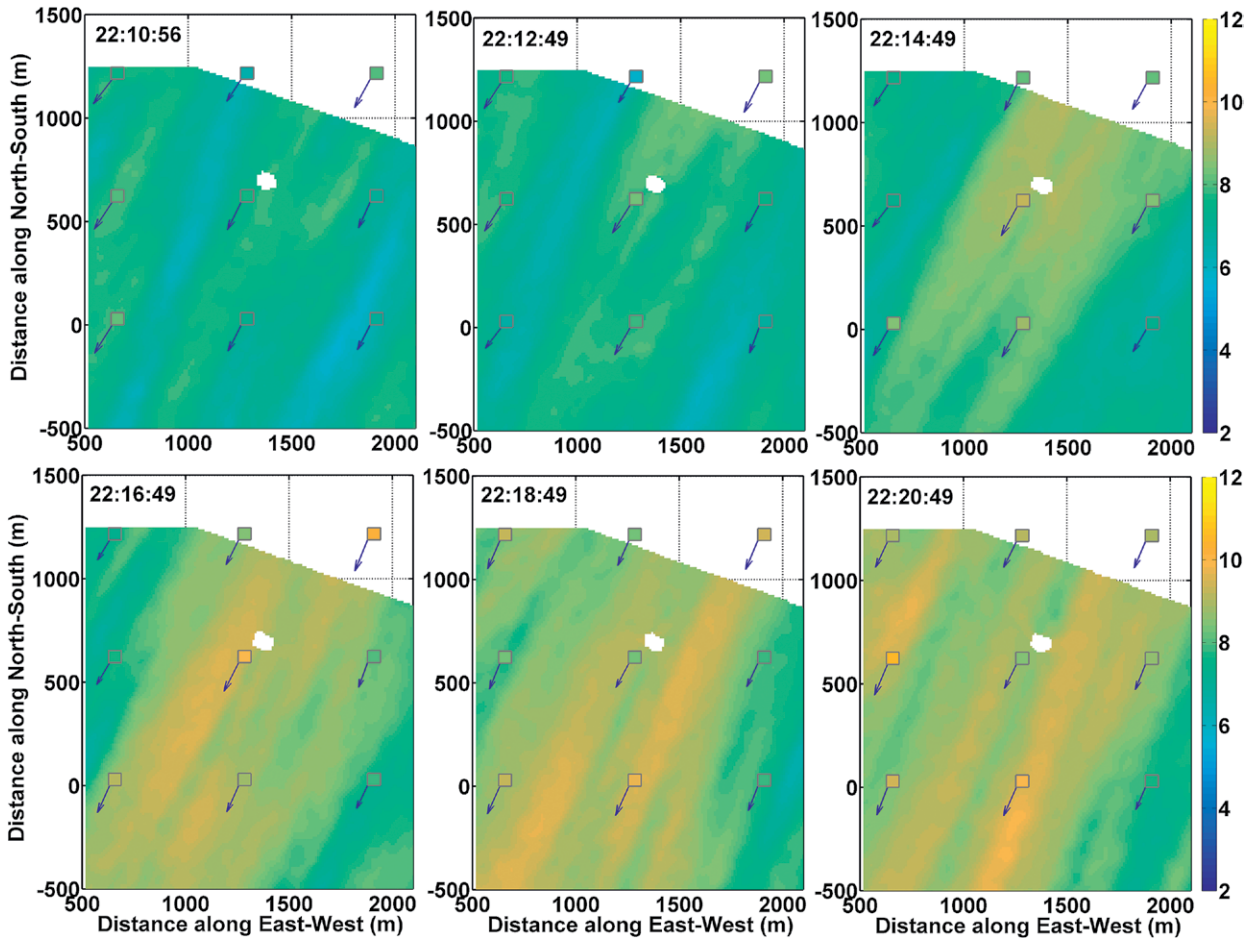


FIG. 13. Wind speed (m s^{-1}) retrievals from the LCB (nine small boxes) overlaid on wind speed retrievals (background color) from the dual-Doppler radars (DDR). Each panel shows a snapshot from one LCB retrieval and a composite of the DDR plane closest in time to the center time of the LCB plane. The boxes representing the lidar retrievals are not to scale. The white space near the center box represents the radar data outage at the location of the tower.

for the height range covered by the RASS within the tower interval (0–300 m) showed the best R^2 between the radiometers and tower (0.89) followed by the RASS 915-MHz profiler and tower (0.81) with the RASS 449-MHz profiler and tower giving a correlation of 0.6 (perhaps lower because of the larger sample volume of the 449-MHz profiler), demonstrating that MWRs provide accurate assessments of atmospheric stability in the atmospheric boundary layer.

DATA ACCESS AND CASE STUDIES OF INTEREST. To facilitate access to all the data collected during XPIA, the DOE Atmosphere to Electrons (A2e) initiative has established a data access portal (<https://a2e.energy.gov/projects/xpia>). Several of the instrument datasets have established online data catalogs for viewing the datasets in graphical format; these are listed in the supplemental material.

Beyond the instrumentation evaluations discussed here, XPIA documented several meteorological case studies ideal for challenging and improving numerical models at both the mesoscale and large-eddy simulation scale. Specific phenomena, such as nocturnal low-level jets and downslope flows, were captured at coarse scales (profilers and soundings) and fine scales (tower measurements, profiling lidar, and scanning radar and lidar).

Case studies ideal for wind energy applications would incorporate wind speeds in excess of 3 m s^{-1} (typical wind turbine cut-in speed) and a strong diurnal variation in stability (representative of onshore North American wind farms). We prioritize the following cases:

- 1400 UTC 16 March–2200 UTC 17 March: This time period captures a strong northeasterly 15 m s^{-1} nocturnal low-level jet (2300 UTC 16

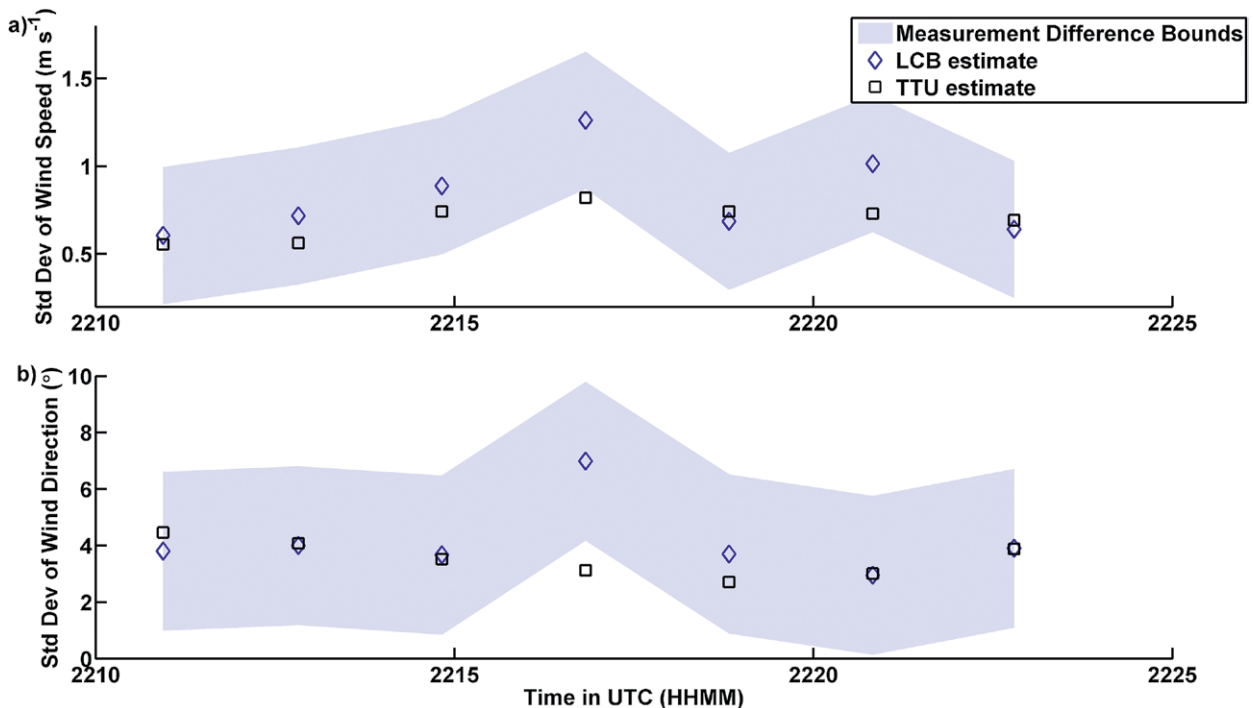


FIG. 14. Spatial variability estimates from the LCB pattern and TTU dual-Doppler Ka-band radar retrievals during the 15-min period of overlap. Comparison of the variability in (a) wind speed and (b) wind direction. The blue envelope defines the measurement difference bounds as discussed in the text.

March to 0400 UTC 17 March), strong daytime temperature variation, and includes seven sounding profiles, 6 h of dual-Doppler radar virtual towers, and excellent visibility provided by the profiling lidars.

- 0000 UTC 2 April–0600 UTC 3 April: The development of a westerly drainage flow jet was disrupted by an intrusion of cold air from the northeast around 0240 UTC, well documented by LCB lidar scanning from 0240 to 0830 UTC. Later development of a neutral boundary layer under thick cloud cover and snowfall was also documented with the LCB from 1800 to 2230 UTC. Radar data are available from two periods, 2023–2054 UTC 2 April, and later document the wake of the tower and a 14 m s^{-1} LLJ from 2140 UTC 2 April to 0400 UTC 3 April.
- 0000 UTC 24 April–1800 UTC 25 April: This time period, marked by clouds and considerable wind speed and direction variability associated with veering, includes several hours of 3D volumes of winds from scanning lidars in stable (0000–0630 UTC 24 April, southerly to westerly), convective (1930 UTC 24 April–0240 UTC 25 April, northwesterly), stable (0530–0900 UTC 25 April, easterly to southeasterly), and convective (1530–1700 UTC 25 April, easterly to

southeasterly) conditions. Soundings are not available during this time, and winds exceed 4 m s^{-1} primarily in stable conditions.

Other time periods in the XPIA dataset contain phenomena of interest, such as low-level jets, density flows, and clear-air vortices.

SUMMARY. In this paper, we present initial results from the eXperimental Planetary boundary layer Instrumentation Assessment (XPIA) campaign at the Boulder Atmospheric Observatory (BAO), held 2 March–31 May 2015. Designed to assess instrumentation capabilities for quantifying the complex flows within wind farms, XPIA employed numerous scanning lidars, scanning radars, profiling lidars, and radiometers, as well as radiosondes, radar wind profilers, and a heavily instrumented 300-m meteorological tower. This breadth of instrumentation was required to assess the accuracy of the instrumentation and to test new instrumentation strategies to be deployed in future wind plant experiments. Strengths of the radar systems used here include high scan rates, large domain coverage, and availability during most precipitation events, but they struggle at times to provide data during periods with limited atmospheric scatterers. In contrast, for the deployment geometry tested here, the lidars have

slower scan rates and less range but provide more data during most nonprecipitating atmospheric conditions.

Comparisons of scanning lidar and scanning radar velocity retrievals of point “stares” and virtual towers to measurements from sonic anemometers confirm the ability of these techniques to reliably provide horizontal wind speed and wind direction with small errors. Vertical velocity estimates have greater uncertainty. By comparing retrievals to the 300-m tower measurements, we find that the vertical velocity uncertainty improves as the elevation angle increases. Allowing for longer measurement accumulation times remedies some error.

Volumetric data from scanning instruments can provide a powerful tool for evaluating simulations, and XPIA developed scanning strategies to compare volumes from the rapidly scanning radars with a large checkerboard (LCB) volume collected from the lidars. The LCB compares well to volumes collected with the faster-scanning dual-Doppler Ka-band radar (DDR): although the LCB suggests higher spatial variability than the radar estimates, the RMSE between the two approaches is smaller than the spatial variability of the winds. We conclude that the LCB technique captures spatial variability similar to the DDR retrievals, but with less detail.

As well as for research into flows around wind turbines or wind plants, coordinated scans using multiple lidars or dual radars have applications in wind energy resource assessment, plant operations, and power performance testing. The results from XPIA show that it is possible to implement lidar scans that can accurately measure wind speeds and directions at multiple points in a 1.6 km × 1.6 km plane (the LCB approach), which is a step change from the data that are available today. These approaches could be highly valuable in complex flow conditions, where traditional vertical profiling devices have higher uncertainty (Clifton et al. 2015).

Beyond winds, XPIA explored measurements of temperature profiles and turbulence dissipation. Because atmospheric stability influences wind farm

performance and the behavior of wind turbine wakes, the quantification of atmospheric stability within wind farms is a critical measurement. The XPIA evaluations of microwave radiometer estimates of temperature profiles occurred throughout the diurnal cycle in a wide range of synoptic conditions, and they show that radiometer measurements offer accurate temperature profile measurements especially in the lower boundary layer. Similarly, estimates of turbulence dissipation rate within wind farms are typically available only with specialized in situ instrumentation (e.g., Lundquist and Bariteau 2015), but XPIA results suggest that radar wind profilers can also provide estimates of dissipation for the improvement of mesoscale numerical weather prediction models.

Results from the XPIA campaign and others suggest promise for measuring inflow and outflow from a wind turbine. With careful consideration of instrumentation capabilities, local weather conditions, and coordinated postprocessing, it is possible to obtain wind and thermodynamic data with spatial and temporal resolution at the scales relevant for wind turbine inflow and outflow studies. This information will be invaluable for understanding and improving the performance of wind turbines and wind plants.

Our results also have implications for boundary layer meteorological studies. Therefore, it is essential that the techniques and methods that have been

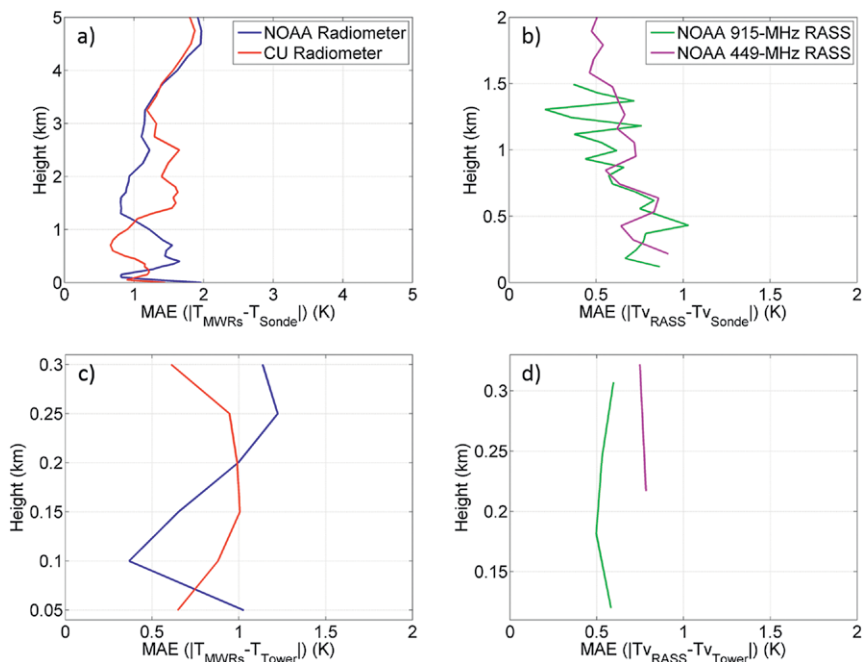


FIG. 15. Profiles of mean absolute error (MAE) between (a) radiometers and radiosondes, (b) RASS and radiosondes, (c) radiometers and tower, and (d) RASS and tower. All data available during the XPIA experiment were included.

demonstrated through XPIA are also communicated to the wider wind energy and meteorology communities; to this end, results are being published here (BAMS), discussed in detail in an upcoming National Renewable Energy Laboratory (NREL) Technical Report, published in a special edition of *Atmospheric Measurement Techniques*, and will be shared via the International Energy Agency (IEA) Implementing Agreement for Co-operation in the Research, Development, and Deployment of Wind Energy Systems (IEA Wind) Task 32 on wind lidar. The XPIA dataset is available to the public online (<https://a2e.energy.gov/projects/xpia>) to enable subsequent evaluations and simulations of the detailed case studies that incorporate data from a rich breadth of instrumentation.

ACKNOWLEDGMENTS. We express great appreciation to the numerous individuals and organizations that assisted with field deployments, including Bruce Bartram, Duane Hazen, Tom Ayers, Jesse Leach, Paul Johnston, the Lefthand Water District, Erie High School, and the St. Vrain School District. We express appreciation to the NOAA/Earth System Research Laboratory/Physical Science Division for supporting the deployment of XPIA instrumentation at the BAO facility and to the National Science Foundation for supporting the CABL deployments (www.eol.ucar.edu/field_projects/cabl). We also acknowledge Drs. Melissa Nigro and Derek Brown at the University of Colorado Boulder for incorporating XPIA/CABL data in their classrooms. We would like to acknowledge the operational, technical, and scientific support provided by NCAR's Earth Observing Laboratory, sponsored by the National Science Foundation. Partial support for the UMBC deployments was provided by the Maryland Energy Administration. Partial support for the UTD lidar and its deployment were provided by UTD institutional funds. NREL is a national laboratory of the U.S. Department of Energy, Office of Energy Efficiency and Renewable Energy, operated by the Alliance for Sustainable Energy, LLC. Funding for this work was provided by the U.S. Department of Energy, Office of Energy Efficiency and Renewable Energy, Wind and Water Power Technologies Office, and by NOAA's Earth System Research Laboratory. Surface flux measurements were supported by NSF Climate and Large-Scale Dynamics (AGS-0955841) as part of the CAREER program. The NOAA dissipation work was funded by the National Research Council's Research Associateship Program. The TTU measurement and analysis effort was provided through a contract with Sandia National Laboratories with funding from the U.S. Department of Energy Wind and Water Power Technologies Office.

REFERENCES

- Aitken, M. L., and J. K. Lundquist, 2014: Utility-scale wind turbine wake characterization using nacelle-based long-range scanning lidar. *J. Atmos. Oceanic Technol.*, **31**, 1529–1539, doi:10.1175/JTECH-D-13-00218.1.
- , M. E. Rhodes, and J. K. Lundquist, 2012: Performance of a wind-profiling lidar in the region of wind turbine rotor disks. *J. Atmos. Oceanic Technol.*, **29**, 347–355, doi:10.1175/JTECH-D-11-00033.1.
- , R. M. Banta, Y. L. Pichugina, and J. K. Lundquist, 2014: Quantifying wind turbine wake characteristics from scanning remote sensor data. *J. Atmos. Oceanic Technol.*, **31**, 765–787, doi:10.1175/JTECH-D-13-00104.1.
- Archer, C. L., and Coauthors, 2014: Meteorology for coastal/offshore wind energy in the United States: Recommendations and research needs for the next 10 years. *Bull. Amer. Meteor. Soc.*, **95**, 515–519, doi:10.1175/BAMS-D-13-00108.1.
- Banta, R. M., R. K. Newsom, J. K. Lundquist, Y. L. Pichugina, R. L. Coulter, and L. Mahrt, 2002: Nocturnal low-level jet characteristics over Kansas during CASES-99. *Bound.-Layer Meteor.*, **105**, 221–252, doi:10.1023/A:1019992330866.
- , Y. L. Pichugina, and W. A. Brewer, 2006: Turbulent velocity-variance profiles in the stable boundary layer generated by a nocturnal low-level jet. *J. Atmos. Sci.*, **63**, 2700–2719, doi:10.1175/JAS3776.1.
- , and Coauthors, 2015: 3D volumetric analysis of wind turbine wake properties in the atmosphere using high-resolution Doppler lidar. *J. Atmos. Oceanic Technol.*, **32**, 904–914, doi:10.1175/JTECH-D-14-00078.1.
- Barthelmie, R. J., S. T. Frandsen, M. N. Nielsen, S. C. Pryor, P.-E. Rethore, and H. E. Jørgensen, 2007: Modelling and measurements of power losses and turbulence intensity in wind turbine wakes at Middelgrunden offshore wind farm. *Wind Energy*, **10**, 517–528, doi:10.1002/we.238.
- Berg, J., N. Vasiljević, M. Kelly, G. Lea, and M. Courtney, 2015: Addressing spatial variability of surface-layer wind with long-range WindScanners. *J. Atmos. Oceanic Technol.*, **32**, 518–527, doi:10.1175/JTECH-D-14-00123.1.
- Bhaganagar, K., and M. Debnath, 2015: The effects of mean atmospheric forcings of the stable atmospheric boundary layer on wind turbine wake. *J. Renewable Sustainable Energy*, **7**, 013124, doi:10.1063/1.4907687.
- Bianco, L., D. Cimini, F. S. Marzano, and R. Ware, 2005: Combining microwave radiometer and wind profiler radar measurements for high-resolution atmospheric

- humidity profiling. *J. Atmos. Oceanic Technol.*, **22**, 949–965, doi:10.1175/JTECH1771.1.
- , D. Gattas, and J. M. Wilczak, 2013: Implementation of a Gabor transform data quality-control algorithm for UHF wind profiling radars. *J. Atmos. Oceanic Technol.*, **30**, 2697–2703, doi:10.1175/JTECH-D-13-00089.1.
- , K. Friedrich, J. Wilczak, D. Hazen, D. Wolfe, R. Delgado, S. Oncley, and J. K. Lundquist, 2016: Assessing atmospheric profiles from microwave radiometers and radio acoustic sounding systems for wind energy applications. *Atmos. Meas. Tech. Discuss.*, doi:10.5194/amt-2016-321.
- Bingöl, F., J. Mann, and D. Foussekis, 2009: Conically scanning lidar error in complex terrain. *Meteor. Z.*, **18**, 189–195, doi:10.1127/0941-2948/2009/0368.
- , —, and G. C. Larsen, 2010: Light detection and ranging measurements of wake dynamics part I: One-dimensional scanning. *Wind Energy*, **13**, 51–61, doi:10.1002/we.352.
- Carbajo Fuertes, F. C., G. V. Iungo, and F. Porté-Agel, 2014: 3D turbulence measurements using three synchronous wind lidars: Validation against sonic anemometry. *J. Atmos. Oceanic Technol.*, **31**, 1549–1556, doi:10.1175/JTECH-D-13-00206.1.
- Cermak, J. E., and J. D. Horn, 1968: Tower shadow effect. *J. Geophys. Res.*, **73**, 1869–1876, doi:10.1029/JB073i006p01869.
- Choukulkar, A., R. Calhoun, B. Billings, and J. D. Doyle, 2012: A modified optimal interpolation technique for vector retrieval for coherent Doppler LIDAR. *IEEE Geosci. Remote Sens. Lett.*, **9**, 1132–1136, doi:10.1109/LGRS.2012.2191762.
- Churchfield, M. J., S. Lee, J. Michalakes, and P. J. Moriarty, 2012: A numerical study of the effects of atmospheric and wake turbulence on wind turbine dynamics. *J. Turbul.*, **13**, N14, doi:10.1080/14685248.2012.668191.
- Cimini, D., and Coauthors, 2011: Thermodynamic atmospheric profiling during the 2010 Winter Olympics using ground-based microwave radiometry. *IEEE Trans. Geosci. Remote Sens.*, **49**, 4959–4969, doi:10.1109/TGRS.2011.2154337.
- Clifton, A., and Coauthors, 2015: Remote sensing of complex flows by Doppler wind lidar: Issues and preliminary recommendations. National Renewable Energy Laboratory Tech. Rep. NREL/TP-5000-64634, 42 pp. [Available online at www.nrel.gov/docs/fy16osti/64634.pdf.]
- Cui, M., D. Ke, Y. Sun, D. Gan, J. Zhang, and B.-M. Hodge, 2015: Wind power ramp event forecasting using a stochastic scenario generation method. *IEEE Trans. Sustainable Energy*, **6**, 422–433, doi:10.1109/TSTE.2014.2386870.
- Dasgupta, B. and T. S. Mruthyunjayab, 2000: The Stewart Platform Manipulator: A review. *Mech. Mach. Theory*, **35**, 15–40, doi:10.1016/S0094-114X(99)00006-3.
- Debnath, M., and Coauthors, 2016: Vertical profiles of the 3D wind velocity retrieved from multiple wind LiDARs performing triple range-height-indicator scans. *Atmos. Meas. Tech. Discuss.*, doi:10.5194/amt-2016-164.
- Dörenkämper, M., B. Witha, G. Steinfeld, D. Heinemann, and M. Kühn, 2015: The impact of stable atmospheric boundary layers on wind-turbine wakes within offshore wind farms. *J. Wind Eng. Ind. Aerodyn.*, **144**, 146–153, doi:10.1016/j.jweia.2014.12.011.
- España, G., S. Aubrun, S. Loyer, and P. Devinant, 2011: Spatial study of the wake meandering using modelled wind turbines in a wind tunnel. *Wind Energy*, **14**, 923–937, doi:10.1002/we.515.
- Fitch, A. C., J. K. Lundquist, and J. B. Olson, 2013: Mesoscale influences of wind farms throughout a diurnal cycle. *Mon. Wea. Rev.*, **141**, 2173–2198, doi:10.1175/MWR-D-12-00185.1.
- Friedrich, K., J. K. Lundquist, M. Aitken, E. A. Kalina, and R. F. Marshall, 2012: Stability and turbulence in the atmospheric boundary layer: A comparison of remote sensing and tower observations. *Geophys. Res. Lett.*, **39**, L03801, doi:10.1029/2011GL050413.
- Gottschall, J., and J. Peinke, 2008: How to improve the estimation of power curves for wind turbines. *Environ. Res. Lett.*, **3**, 015005, doi:10.1088/1748-9326/3/1/015005.
- Grund, C. J., R. M. Banta, J. L. George, J. N. Howell, M. J. Post, R. A. Richter, and A. M. Weickmann, 2001: High-resolution Doppler lidar for boundary layer and cloud research. *J. Atmos. Oceanic Technol.*, **18**, 376–393, doi:10.1175/1520-0426(2001)018<0376:HRDLFB>2.0.CO;2.
- Gunter, W. S., J. L. Schroeder, and B. D. Hirth, 2015: Validation of dual-Doppler wind profiles with in situ anemometry. *J. Atmos. Oceanic Technol.*, **32**, 943–960, doi:10.1175/JTECH-D-14-00181.1.
- Hamada, M., P. Dérian, C. F. Mauzey, and S. D. Mayor, 2016: Optimization of the cross-correlation algorithm for two-component wind field estimation from single aerosol lidar data and comparison with Doppler lidar. *J. Atmos. Oceanic Technol.*, **33**, 81–101, doi:10.1175/JTECH-D-15-0009.1.
- Hill, M., R. Calhoun, H. J. S. Fernando, A. Wieser, A. Dörnbrack, M. Weissmann, G. Mayr, and R. Newsom, 2010: Coplanar Doppler lidar retrieval of rotors from T-REX. *J. Atmos. Sci.*, **67**, 713–729, doi:10.1175/2009JAS3016.1.
- Hirth, B. D., and J. L. Schroeder, 2013: Documenting wind speed and power deficits behind a utility-scale

- wind turbine. *J. Appl. Meteor. Climatol.*, **52**, 39–46, doi:10.1175/JAMC-D-12-0145.1.
- , —, W. S. Gunter, and J. G. Guynes, 2015: Coupling Doppler radar-derived wind maps with operational turbine data to document wind farm complex flows. *Wind Energy*, **18**, 529–540, doi:10.1002/we.1701.
- Hocking, W. K., 1985: Measurement of turbulent energy dissipation rates in the middle atmosphere by radar techniques: A review. *Radio Sci.*, **20**, 1403–1422, doi:10.1029/RS020i006p01403.
- Högström, U., D. N. Asimakopoulou, H. Kambezidis, C. G. Helmis, and A. Smedman, 1988: A field study of the wake behind a 2 MW wind turbine. *Atmos. Environ.*, **22**, 803–820, doi:10.1016/0004-6981(88)90020-0.
- Horst, T. W., S. R. Semmer, and I. Bogoev, 2016: Evaluation of mechanically-aspirated temperature/relative humidity radiation shields. *18th Symp. on Meteorological Observation and Instrumentation*, New Orleans, LA, Amer. Meteor. Soc., 6B.4. [Available online at <https://ams.confex.com/ams/96Annual/webprogram/Paper286839.html>.]
- Howard, K. B., A. Singh, F. Sotiropoulos, and M. Guala, 2015: On the statistics of wind turbine wake meandering: An experimental investigation. *Phys. Fluids*, **27**, 075103, doi:10.1063/1.4923334.
- IEC, 2005: Wind turbines—Part 12-1: Power performance measurements of electricity producing wind turbines. International Electrotechnical Commission 61400-12-1:2005(E), 90 pp. [Available online at ftp://ftp.ee.polyu.edu.hk/wclo/Ext/OAP/IEC61400part12_1_WindMeasurement.pdf.]
- Jungo, G. V., and F. Porté-Agel, 2014: Volumetric lidar scanning of wind turbine wakes under convective and neutral atmospheric stability regimes. *J. Atmos. Oceanic Technol.*, **31**, 2035–2048, doi:10.1175/JTECH-D-13-00252.1.
- , Y.-T. Wu, and F. Porté-Agel, 2013: Field measurements of wind turbine wakes with lidars. *J. Atmos. Oceanic Technol.*, **30**, 274–287, doi:10.1175/JTECH-D-12-00051.1.
- Jacoby-Koaly, S., B. Campistron, S. Bernard, B. Bénech, F. Ardhuin-Girard, J. Dessens, E. Dupont, and B. Carissimo, 2002: Turbulent dissipation rate in the boundary layer via UHF wind profiler Doppler spectral width measurements. *Bound.-Layer Meteor.*, **103**, 361–389, doi:10.1023/A:1014985111855.
- Jordan, J. R., R. J. Latatits, and D. A. Carter, 1997: Removing ground and intermittent clutter contamination from wind profiler signals using wavelet transforms. *J. Atmos. Oceanic Technol.*, **14**, 1280–1297, doi:10.1175/1520-0426(1997)014<1280:RGAI CC>2.0.CO;2.
- Kaimal, J. C., and J. E. Gaynor, 1983: The Boulder Atmospheric Observatory. *J. Climate Appl. Meteor.*, **22**, 863–880, doi:10.1175/1520-0450(1983)022<0863:TBAO>2.0.CO;2.
- Käsler, Y., S. Rahm, R. Simmet, and M. Kühn, 2010: Wake measurements of a multi-MW wind turbine with coherent long-range pulsed Doppler wind lidar. *J. Atmos. Oceanic Technol.*, **27**, 1529–1532, doi:10.1175/2010JTECHA1483.1.
- Klein, P., and Coauthors, 2015: LABEL: A multi-institutional, student-led, atmospheric boundary layer experiment. *Bull. Amer. Meteor. Soc.*, **96**, 1743–1764, doi:10.1175/BAMS-D-13-00267.1.
- Krishnamurthy, R., A. Choukulkar, R. Calhoun, J. Fine, A. Oliver, and K. S. Barr, 2013: Coherent Doppler lidar for wind farm characterization. *Wind Energy*, **16**, 189–206, doi:10.1002/we.539.
- Kumer, V.-M., J. Reuder, B. Svardal, C. Sætre, and P. Eecen, 2015: Characterisation of single wind turbine wakes with static and scanning WINTWEX-W LiDAR data. *Energy Procedia*, **80**, 245–254, doi:10.1016/j.egypro.2015.11.428.
- Lehmann, V., and G. Teschke, 2008: Advanced intermittent clutter filtering for radar wind profiler: Signal separation through a Gabor frame expansion and its statistics. *Ann. Geophys.*, **26**, 759–783, doi:10.5194/angeo-26-759-2008.
- Lundquist, J. K., and L. Bariteau, 2015: Dissipation of turbulence in the wake of a wind turbine. *Bound.-Layer Meteor.*, **154**, 229–241, doi:10.1007/s10546-014-9978-3.
- , M. J. Churchfield, S. Lee, and A. Clifton, 2015: Quantifying error of lidar and sodar Doppler beam swinging measurements of wind turbine wakes using computational fluid dynamics. *Atmos. Meas. Tech.*, **8**, 907–920, doi:10.5194/amt-8-907-2015.
- Mann, J., and Coauthors, 2008: Comparison of 3D turbulence measurements using three staring wind lidars and a sonic anemometer. *IOP Conf. Ser.: Earth Environ. Sci.*, **1**, 012012, doi:10.1088/1755-1307/1/1/012012.
- Mather, J. H., and J. W. Voyles, 2013: The ARM Climate Research Facility: A review of structure and capabilities. *Bull. Amer. Meteor. Soc.*, **94**, 377–392, doi:10.1175/BAMS-D-11-00218.1.
- Mathisen, J.-P., 2013: Measurement of wind profile with a buoy mounted lidar. Fugro, 19 pp. [Available online at www.sintef.no/globalassets/project/deepwind-2013/deepwind-presentations-2013/c2/mathisen-j-p_fugro-oceanor.pdf.]
- May, P. T., K. P. Moran, and R. G. Strauch, 1989: The accuracy of RASS temperature measurements. *J. Appl. Meteor.*, **28**, 1329–1335, doi:10.1175/1520-0450(1989)028<1329:TAORTM>2.0.CO;2.

- Mayor, S. D., and E. W. Eloranta, 2001: Two-dimensional vector wind fields from volume imaging lidar data. *J. Appl. Meteor.*, **40**, 1331–1346, doi:10.1175/1520-0450(2001)040<1331:TDVWFF>2.0.CO;2.
- McCaffrey, K., L. Bianco, P. Johnston, and J. M. Wilczak, 2016a: Vertical velocity variance measurements from wind profiling radars. *Atmos. Meas. Tech. Discuss.*, doi:10.5194/amt-2016-299.
- , and Coauthors, 2016b: Identification of tower wake distortions using sonic anemometer and lidar measurements. *Atmos. Meas. Tech. Discuss.*, doi:10.5194/amt-2016-179.
- , L. Bianco, P. Johnston, and J. M. Wilczak, 2017: Effects of post-processing techniques on radar spectral width and vertical velocity variance measurements. *Atmos. Meas. Tech.*, in press.
- Mikkelsen, T., and Coauthors, 2013: A spinner-integrated wind lidar for enhanced wind turbine control. *Wind Energy*, **16**, 625–643, doi:10.1002/we.1564.
- Mirocha, J. D., B. Kosovic, M. L. Aitken, and J. K. Lundquist, 2014: Implementation of a generalized actuator disk wind turbine model into the weather research and forecasting model for large-eddy simulation applications. *J. Renewable Sustainable Energy*, **6**, 013104, doi:10.1063/1.4861061.
- , D. A. Rajewski, N. Marjanovic, J. K. Lundquist, B. Kosović, C. Draxl, and M. J. Churchfield, 2015: Investigating wind turbine impacts on near-wake flow using profiling lidar data and large-eddy simulations with an actuator disk model. *J. Renewable Sustainable Energy*, **7**, 043143, doi:10.1063/1.4928873.
- Muñoz-Esparza, D., B. Kosović, J. Mirocha, and J. van Beeck, 2014: Bridging the transition from mesoscale to microscale turbulence in numerical weather prediction models. *Bound.-Layer Meteor.*, **153**, 409–440, doi:10.1007/s10546-014-9956-9.
- , —, J. van Beeck, and J. Mirocha, 2015: A stochastic perturbation method to generate inflow turbulence in large-eddy simulation models: Application to neutrally stratified atmospheric boundary layers. *Phys. Fluids*, **27**, 035102, doi:10.1063/1.4913572.
- Newsom, R. K., 2012: Doppler lidar (DL) handbook. DOE/SC-ARM-TR-101, 16 pp. [Available online at www.arm.gov/publications/tech_reports/handbooks/dl_handbook.pdf.]
- , R. Calhoun, D. Ligon, and J. Allwine, 2008: Linearly organized turbulence structures observed over a suburban area by dual-Doppler lidar. *Bound.-Layer Meteor.*, **127**, 111–130, doi:10.1007/s10546-007-9243-0.
- Orlando, S., A. Bale, and D. A. Johnson, 2011: Experimental study of the effect of tower shadow on anemometer readings. *J. Wind Eng. Ind. Aerodyn.*, **99**, 1–6, doi:10.1016/j.jweia.2010.10.002.
- Pearson, G., F. Davies, and C. Collier, 2009: An analysis of the performance of the UFAM pulsed Doppler lidar for observing the boundary layer. *J. Atmos. Oceanic Technol.*, **26**, 240–250, doi:10.1175/2008JTECHA1128.1.
- Pichugina, Y. L., S. C. Tucker, R. M. Banta, W. A. Brewer, N. D. Kelley, B. J. Jonkman, and R. K. Newsom, 2008: Horizontal-velocity and variance measurements in the stable boundary layer using Doppler lidar: Sensitivity to averaging procedures. *J. Atmos. Oceanic Technol.*, **25**, 1307–1327, doi:10.1175/2008JTECHA988.1.
- , R. M. Banta, W. A. Brewer, S. P. Sandberg, and R. M. Hardesty, 2012: Doppler lidar-based wind-profile measurement system for offshore wind-energy and other marine boundary layer applications. *J. Appl. Meteor. Climatol.*, **51**, 327–349, doi:10.1175/JAMC-D-11-040.1.
- Porté-Agel, F., Y.-T. Wu, H. Lu, and R. J. Conzemius, 2011: Large-eddy simulation of atmospheric boundary layer flow through wind turbines and wind farms. *J. Wind Eng. Ind. Aerodyn.*, **99**, 154–168, doi:10.1016/j.jweia.2011.01.011.
- Rajewski, D. A., 2013: CWEX (Crop/Wind-Energy Experiment): Measurements of the interaction between crop agriculture and wind power. Ph.D. dissertation, The Iowa State University, 181 pp. [Available online at <http://lib.dr.iastate.edu/etd/13404/>.]
- Rhodes, M. E., and J. K. Lundquist, 2013: The effect of wind-turbine wakes on summertime US Midwest atmospheric wind profiles as observed with ground-based Doppler lidar. *Bound.-Layer Meteor.*, **149**, 85–103, doi:10.1007/s10546-013-9834-x.
- Sanz Rodrigo, J., F. Borbón Guillén, P. Gómez Arranz, M. S. Courtney, R. Wagner, and E. Dupont, 2013: Multi-site testing and evaluation of remote sensing instruments for wind energy applications. *Renewable Energy*, **53**, 200–210, doi:10.1016/j.renene.2012.11.020.
- Sathe, A., and J. Mann, 2013: A review of turbulence measurements using ground-based wind lidars. *Atmos. Meas. Tech.*, **6**, 3147–3167, doi:10.5194/amt-6-3147-2013.
- , —, J. Gottschall, and M. S. Courtney, 2011: Can wind lidars measure turbulence? *J. Atmos. Oceanic Technol.*, **28**, 853–868, doi:10.1175/JTECH-D-10-05004.1.
- , —, T. Barlas, W. A. A. M. Bierbooms, and G. J. W. van Bussel, 2013: Influence of atmospheric stability on wind turbine loads: Atmospheric stability and loads. *Wind Energy*, **16**, 1013–1032, doi:10.1002/we.1528.

- Schlipf, D., D. J. Schlipf, and M. Kühn, 2013: Nonlinear model predictive control of wind turbines using LIDAR: Nonlinear model predictive control of wind turbines using LIDAR. *Wind Energy*, **16**, 1107–1129, doi:10.1002/we.1533.
- Smalikho, I. N., V. A. Banakh, Y. L. Pichugina, W. A. Brewer, R. M. Banta, J. K. Lundquist, and N. D. Kelley, 2013: Lidar investigation of atmosphere effect on a wind turbine wake. *J. Atmos. Oceanic Technol.*, **30**, 2554–2570, doi:10.1175/JTECH-D-12-00108.1.
- Stawiarski, C., K. Träumner, C. Knigge, and R. Calhoun, 2013: Scopes and challenges of dual-Doppler lidar wind measurements—An error analysis. *J. Atmos. Oceanic Technol.*, **30**, 2044–2062, doi:10.1175/JTECH-D-12-00244.1.
- Sumner, J., and C. Masson, 2006: Influence of atmospheric stability on wind turbine power performance curves. *J. Sol. Energy Eng.*, **128**, 531–538, doi:10.1115/1.2347714.
- Trabucchi, D., J.-J. Trujillo, J. Schneemann, M. Bitter, and M. Kühn, 2015: Application of staring lidars to study the dynamics of wind turbine wakes. *Meteor. Z.*, **24**, 557–564, doi:10.1127/metz/2014/0610.
- Vanderwende, B. J., and J. K. Lundquist, 2012: The modification of wind turbine performance by statistically distinct atmospheric regimes. *Environ. Res. Lett.*, **7**, 034035, doi:10.1088/1748-9326/7/3/034035.
- , —, M. E. Rhodes, E. S. Takle, and S. L. Irvin, 2015: Observing and simulating the summertime low-level jet in central Iowa. *Mon. Wea. Rev.*, **143**, 2319–2336, doi:10.1175/MWR-D-14-00325.1.
- Vasiljević, N., 2014: A time-space synchronization of coherent Doppler scanning lidars for 3D measurements of wind fields. DTU Wind Energy, 177 pp. [Available online at http://orbit.dtu.dk/files/102963702/NVasiljevic_Thesis.pdf.]
- Wainwright, C. E., P. M. Stepanian, P. B. Chilson, R. D. Palmer, E. Fedorovich, and J. A. Gibbs, 2014: A time series sodar simulator based on large-eddy simulation. *J. Atmos. Oceanic Technol.*, **31**, 876–889, doi:10.1175/JTECH-D-13-00161.1.
- Walter, K., C. C. Weiss, A. H. P. Swift, J. Chapman, and N. D. Kelley, 2009: Speed and direction shear in the stable nocturnal boundary layer. *J. Sol. Energy Eng.*, **131**, 011013, doi:10.1115/1.3035818.
- Ware, R., R. Carpenter, J. Güldner, J. Liljegren, T. Nehr Korn, F. Solheim, and F. Vandenberghe, 2003: A multichannel radiometric profiler of temperature, humidity, and cloud liquid. *Radio Sci.*, **38**, 8079, doi:10.1029/2002RS002856.
- , and Coauthors, 2013: Thermodynamic and liquid profiling during the 2010 Winter Olympics. *Atmos. Res.*, **132–133**, 278–290, doi:10.1016/j.atmosres.2013.05.019.
- Wharton, S., and J. K. Lundquist, 2012: Atmospheric stability affects wind turbine power collection. *Environ. Res. Lett.*, **7**, 014005, doi:10.1088/1748-9326/7/1/014005.
- Wilczak, J. M., S. P. Oncley, and S. A. Stage, 2001: Sonic anemometer tilt correction algorithms. *Bound.-Layer Meteor.*, **99**, 127–150, doi:10.1023/A:1018966204465.
- Wiser, R. H., and Coauthors, 2015: 2014 wind technologies market report. U.S. Department of Energy, 81 pp. [Available online at <http://energy.gov/sites/prod/files/2015/08/f25/2014-Wind-Technologies-Market-Report-8.7.pdf>.]